3-7-2008

Environmental Effects on Nano-Wear of Gold and KBr Single Crystal

Megan Pendergast
University of South Florida

Scholar Commons Citation

Pendergast, Megan, "Environmental Effects on Nano-Wear of Gold and KBr Single Crystal" (2008). *Graduate Theses and Dissertations.* https://scholarcommons.usf.edu/etd/447

Environmental Effects on Nano-Wear of Gold and KBr Single Crystal

by

Megan Pendergast

A thesis submitted in partial fulfillment
of the requirements for the degree of
Master of Science in Mechanical Engineering
Department of Mechanical Engineering
College of Engineering
University of South Florida

Major Professor: Alex A. Volinsky, Ph.D.
Nathan B. Crane, Ph.D.
Frank Pyrtle, III, Ph.D.

Date of Approval:
March 7, 2008

Keywords: Single crystal ripples, Moisture assisted wear, Scratch testing, Gold pattern formation

DEDICATION

To my grandfather, Monroe Moore, who always instilled in me the importance of an education.

ACKNOWLEDGEMENTS

I would like to thank my advisor, Prof. Alex A. Volinsky, for his guidance and availability while performing my research. I would also like to thank Dr. Marek Szymonski's group at Jagellonian University for allowing me to perform research at their facility and all of their hospitality while I was visiting. I would like to thank my lab members Ramakrishna Gunda, Jayadeep Deva Reddy, Xialou Pang, Nathaniel Waldstein, Viacheslav Kuryachiy, Bobby Shields, and Patrick Waters who were all very helpful to me and available for assistance. This work is supported by the National Science Foundation (CMMI-0631526), the division of Design, Manufacture and Industrial Innovation, and the Marie Curie Host Fellowship for the Transfer of Knowledge under the project "Nano-engineering for Expertise and Development – NEED" within the 6th EU Framework Program. I would like to also acknowledge Hysitron for their vast knowledge of the instrument and all of their assistance in handling my questions.

TABLE OF CONTENTS

LIST OF TABLES

LIST OF FIGURES

Environmental Effects on Nano-Wear of Gold and KBr Single Crystal

Megan Pendergast

ABSTRACT

In order to successfully incorporate the tremendous possibilities of nanoscale applications into devices and manufacturing, significant studies need to be conducted of the properties and mechanics of materials of this small scale. In this thesis, the effect of repeated scanning of KBr, aluminum, and gold was studied by using a nanoindenter and Atomic Force Microscope (AFM) in varying environments. Additional research was performed to study the environmental effects of gold film scratching using a Taber Shear/Scratch Tester.

Scanning of KBr single crystal surface in air with a diamond tip in the Hysitron Triboindenter formed surface ripples 100 nm high, 1 micron apart. It has been observed that the nanoripple's initial height and period increase with the number of repeated scans. The surface ripples form perpendicular to the scanning direction, beginning at the bottom of sloped samples and working their way up the entire scan area. The addition of water to a wear experiment on gold film produced considerably deeper wear areas than its ambient air counterpart in both scanning machines. Scratch testing with a conical diamond tip of 77 μm radius with 125 g normal load also produced deeper wear tracks in water than in ambient air conditions.

Several mechanisms may be responsible for the ripples formation, including dislocation dynamics, chatter, piezo hysteresis and others. Most likely there is a

combination of effects, with a clear differentiation between nanoripple's origination and propagation. Mechanisms responsible for rippling, including system dynamic response and stick slip behavior are investigated. Topography modification appears to be the main result of ambient wear tests at the nanoscale, whereas much higher wear rate and nanoripples are observed in water. It is possible that this moisture is assisting grain fracture and pull off.

CHAPTER 1

INTRODUCTION AND NANOSCALE RESEARCH MOTIVATION

1.1 Nomenclature

Unless otherwise specified, the following nomenclature is used in this thesis:

H – (Pa) Hardness
E – (Pa) Modulus of Elasticity
P – (N) Load
V – (m^3) Volume
x – (m) Distance
μ_s – (unitless) Static coefficient of friction
μ_p – (unitless) Ploughing coefficient of friction
R – (m) Tip radius
τ – (Pa) Shear strength
p – (Pa) Material flow stress
γ – (J/m^2) Work of Adhesion

1.2 The Growth of Nanoscale Applications

As the forefront of technology pushes towards miniaturization and the boom of nanoscale applications takes hold across the world, research in this area also must accommodate the testing scale [1]. Estimated costs in the U.S. attributed to friction and wear are upwards of hundreds of billions of dollars in macroscale applications. Estimated costs in smaller, nanoscale devices like Micro-electrical mechanical systems (MEMS) and Nano-electrical mechanical systems (NEMS) do not even exist because these markets can not even develop until the debilitating issues with friction and wear in moving parts are solved [2]. There is a strong technological push for the lifetime of these devices to be significantly improved; friction and wear being two properties monumental to the device's longevity [3].

Friction and wear have been shown to change when comparing macroscale results to nanoscale. With reference to the generally small size of the components, bulk material physics does not dominate; instead, surface forces play the main role in determining characteristics of the material's reaction [2]. The issue of stiction in MEMS devices at the nanoscale is a heavily researched example of this surface force domination. The field of nanoscale tribological testing, more specifically with the Atomic Force Microscope (AFM) is still in its very early stages in terms of understanding and being able to quantify certain aspects such as tip geometry characterization and force calibration. These processes are not yet standardized so the field of nano tribology still remains largely unresolved [4].

1.3 Wear

Tribological processes like wear and friction occur in instances when sliding and or rolling contact occurs. Wear is the progressive loss of a substance from the surface of a body due to the relative motion between the surfaces. Wear can be chemical (corrosive) or mechanical, but an important often misunderstood fact is that wear is not a material property, rather an effect from an environment to which the material is being exposed [5]. This is why an appropriate method of wear testing is vital for specific applications. In describing wear processes, the main modes are sliding (absence of particles) and abrasive (presence of particles). These modes are not drastically stiff – for example sliding wear can generate debris and thus transform to abrasive wear. Erosive wear is a subcategory of abrasive wear, where particles can be carried to the surface through a gas or liquid stream [6]. A common quantitative description of wear in terms of Volume (V) loss is defined below [7]:

$$V = \frac{kPx}{H} \tag{1}$$

where P is the load, x is the sliding distance, H is the hardness of the material being worn, and k is a dimensionless quantity known as the wear coefficient. This parameter is related to the coefficient of friction between the two materials.

Macroscale wear testing is performed for many different reasons, some simply to obtain an idea of longevity and others to compare materials and different environments of use. The difficulty is that field studies are not always feasible economically or practically. Lab testing is the alternative to studying these conditions, but provides the risk of imperfect recreation; which is also an issue when testing at smaller scales [5]. Traditional solutions to wear and friction at the macroscale include lubrication and bearings. As the dimensional range of interest has shifted to the nano regime, these solutions are not applicable because of the enormous change in surface to volume or mass ratios [8].

1.3.1 Wear Testing

Wear tests can be generally categorized as nondestructive or destructive. The nondestructive tests require immense knowledge in terms of materials' structural properties and also the wear mechanisms involved. The destructive type can be further organized into single pass and multiple pass tests. Single pass tests provide knowledge of the coefficient of friction, whereas multiple passes elucidate how this coefficient of friction changes over time. In a typical wear experiment a hard material is repeatedly scanned over the tested material surface under load. Wear rate is expressed in terms of the removed material depth (or volume) as a function of normal applied load and number of wear cycles. A trench is left in tested material as a result of the wear process [9].

After a wear test many options arise for interpreting the loss of material, depth of wear track and corresponding “wear rate”. Surface topographical measures such as profilometry, AFM, optical microscopy, STM, and SEM are typical micro and nanoscale tools for interpreting wear. A direct measure of the volume change or profilometry can be applicable to larger scale tests. Other characterization can be performed, including electron diffraction, Auger electron spectostropy, or Rutherford backscattering. The idea of wear rate is rather complex and difficult to quantify, as wear is a constantly changing dynamic process, but provides useful knowledge of the friction behavior of the material [5].

1.4 Friction

The simplest model of friction given as the Amontons-Coulomb friction represents the ratio of the friction force (F) to the normal force (N) through a parameter called the coefficient of kinetic friction [10].

$$\mu = \frac{F}{N} \qquad (2)$$

The roughness theory of friction accredited to Tabor attributes the action of friction to asperities, and lower dynamic friction coefficients were explained by the asperities “jumping” over gaps between the surfaces. However, this theory does not account for friction dissipation. Tabor lists three factors that contribute to friction in unlubricated surfaces: 1) The real contact area, 2) the type and strength of the interface bond between the surfaces, and 3) the material’s properties in terms of shear and rupture.

1.4.1 The Hertz Contact Mechanics Model

The Hertz model for single asperity contact requires the knowledge of the contact area, which must be small compared to the dimensions of the body and the radius of curvature of the surfaces. The strain has to be small so linear elasticity is still valid, and only normal pressure is transmitted (no friction), and each body is represented by an elastic half space. To assume that the tip is a perfect sphere, it requires that the contact area be proportional to the 2/3 power of the normal force. Then friction force is proportional to the contact area (assuming no sample damage) and thus too is proportional to the 2/3 power of the normal force. However, most friction versus load graphs obtained from sliding a sharp tip over the surface show a linear relationship, signifying that those tips cannot be modeled as perfect spheres and must have more than single-asperity contact. The environmental effect on the validity of this contact has been shown by Putman in experiments with an Atomic Force Microscope (AFM) in 55% humidity in an environment flooded with N_2 [1]. The ambient experiment showed a non-linear relationship between friction and load, indicating a single asperity contact, where the N_2 flooded vacuum experiment showed a linear relationship indicating multi-asperity contact. This proves that environment plays a large role in the nature of friction, being either single asperity or multi asperity in different environments. The question of why the ambient experiment produced single-asperity contact and the gaseous vacuum experiments did not was answered by the probability of ambient conditions always having a layer of moisture or hydrocarbons present on the surface of the tip and the tested material, essentially, "filling in" the tip roughness, yielding to a single-asperity contact. The opposite is true in the vacuum where surface roughness is not smoothed over by an adsorbed surface layer, producing the multi-asperity contact [1].

1.4.2 Adhesion in Friction

For small contacts, the adhesion of the surfaces plays a substantial role in the frictional values. The model of Johnson, Kendall, and Roberts (JKR) predicts that these adhesive forces can provide deformation (therefore greater contact area) that is larger than what is predicted by the Hertz model. Their equation describes the contact radius (a) between a flat plane and a sphere with adhesion present [11]:

$$a = \left(\frac{R}{E_r} \left(P + 3\gamma\pi R + \sqrt{6\gamma\pi RP + (3\gamma\pi R)^2} \right) \right)^{\frac{1}{3}} \qquad (3)$$

where γ is the work of adhesion, or Dupre's energy. R is the radius of the sphere, E_R is the reduced modulus and P is the normal load.

This model provides a non- zero contact area at zero contact load, and a minimum stable load that corresponds to a non-zero contact area. This minimum load is defined by:

$$P_{c(JKR)} = -\frac{3}{2}\pi\gamma R \tag{4}$$

Four years after the JKR model, the Derjaguin, Muller and Toporov (DMT) model was derived and used the same deformed contact profile as the Hertz model, but a higher load to account for adhesion. In this model, the contact area goes to zero at the pull off force:

$$a = \left(\frac{R}{E_R}(P + 2\gamma\pi R)\right)^{\frac{1}{3}} \tag{5}$$

and $P_{c(DMT)} = -2\pi\gamma R$ (6)

The JKR model also assumes that the area of contact is increased, a parameter not included in the DMT model [13]. Traditionally, the JKR model is suited for softer materials, large radii, and short range, strong adhesive forces while the DMT model is suited for harder materials, smaller radii, with long range adhesive forces [11].

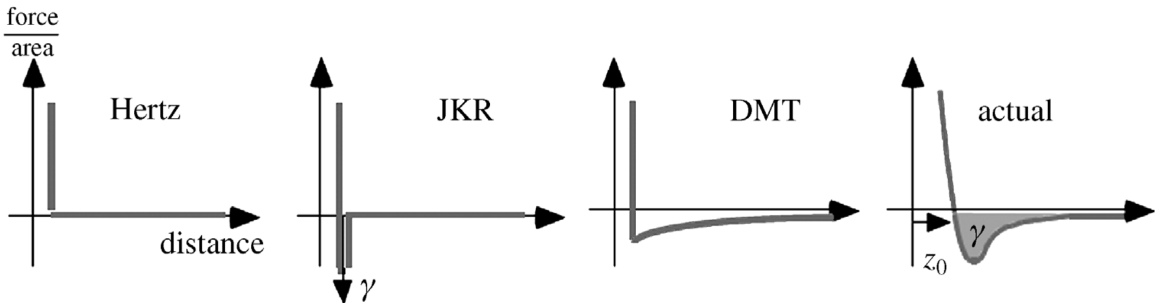

Figure 1.1. Interaction forces versus distance for various models compared to an actual interaction. Reproduced with permission from the Journal of Adhesion Science Technology [11].

A visual summary of the models and their adhesion influences can be seen in Figure 1.1. The Hertz model does not account for any adhesion, while the JKR model accounts for adhesion only within the contact zone. The DMT model shows a longer range effect of adhesion. The actual interaction would have a well corresponding to the work of adhesion, γ.

Lateral forces arise not only from friction but from the sample slope as well. This provides the surface with a lateral force resulting from a component of the normal force [4]. The main differences when comparing large scale friction testing to a smaller scale is the single asperity contact. For the AFM the tip geometry is well defined, and single asperity contact can be achieved, unlike for the large scale friction testing. The standard linear relationship between friction force and normal load is not always applicable at small scales. Some frictional force values can be measured at zero or slightly below zero in AFM measurements - comparable to the tip adhering to the sample, and the relationship is not always linear [10, 14]. An example of some of these measurements on various materials can be seen in Table 1.1.

Table 1.1. Measured adhesion force in an AFM between SiN tip and different materials [15-18].

Material	Adhesion force observed in AFM
Polystyrine	2000 nN
Gold	20 nN
Human hair	25 nN
Silica	15 nN
Titania	12 nN

1.4.3 Stick Slip Friction

As the kinetic coefficient of friction is almost always lower than the static coefficient, it is rare that movement will be perfectly smooth; rather, some "jumpiness" is to be expected [19]. The stick is due to the higher static friction coefficient, and the observed slip is the slide of materials that happens at the lower kinetic friction coefficient. Figure 1.2 is a graphical representation of the two coefficients. A general rule is that the quicker the motion, the less time the static friction is allowed to "stick", and the motion appears to be less jerky [20]. This is why stick slip is observed mainly at lower speeds. This is because the kinetic coefficient of friction is somewhat velocity dependent, and for different loads, and materials, there exists some critical velocity where stick slip is no longer noticeable.

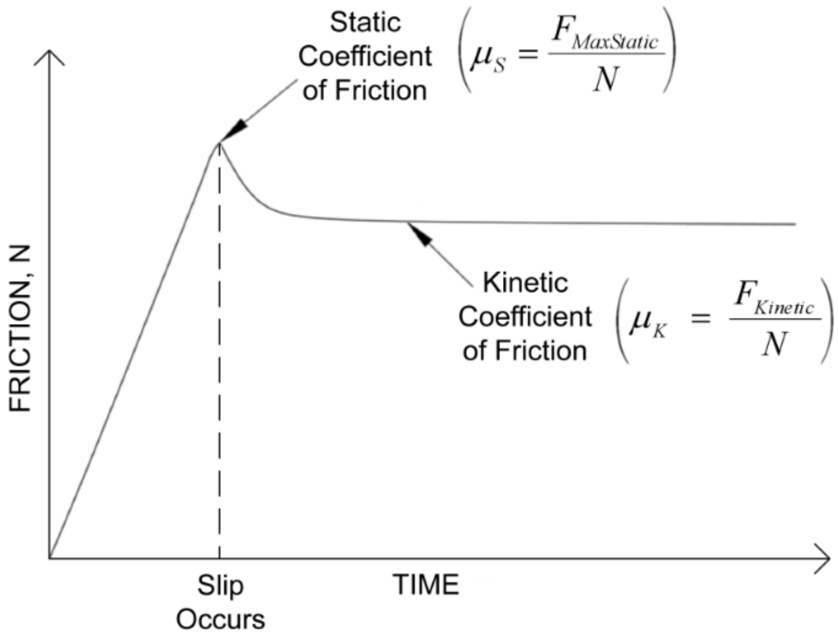

Figure 1.2. Relationship between friction coefficients and load.

Every object has some degree of elasticity, including the indenter and AFM tips. Usually this is small enough that it is unnoticeable, but exists even at a reduced scale.

In modeling this dynamic response, two equations of motion are needed; one to represent the "stick" (zero velocity), and another to represent the "slip":

$$m\frac{d^{2}x}{dt^{2}} + c\frac{dx}{dt} + kx = F_{ts}(\Delta v) \qquad (7)$$

where c is the damping coefficient, m is the mass of the oscillator, k is the cantilever spring constant, x(t) is the displacement of the tip, $F_{ts}(\Delta v)$ is the frictional force between the tip and sample during sliding [21].

In many poorly designed sliding instances, pile up is produced ahead of the motion, thus increasing the friction. This continues to increase until a point of instability is reached and sliding occurs at the lower original friction value. Something must yield to cause this drop in friction, and this type of motion is called spragging [22]. This yielding of material during spragging is associated with plastic deformation [23, 24].

1.5 Instruments for Exploring Wear and Friction Properties

1.5.1 Macroscale Wear Tests

Wear at the macroscale is prominently relevant in engines, especially now when the global push is towards less fuel consumption requiring lighter, smaller parts. Working conditions of modern day engines require extreme temperatures, pressures and speeds. There is a standard wear rate in engines of a few nanometers per hour, elucidating how much effort is put into reducing wear in these parts. Due to the pressure of industry, investigation of wear in unknown regimes, sometimes at the micro and nanoscales is imperative to keep up with the technological advances [3]. There are no standards in wear testing for the AFM or Triboindentor environments - most wear testing is done at the macroscale, however, significant differences can be discovered when experimenting with wear on a smaller microscopic scale.

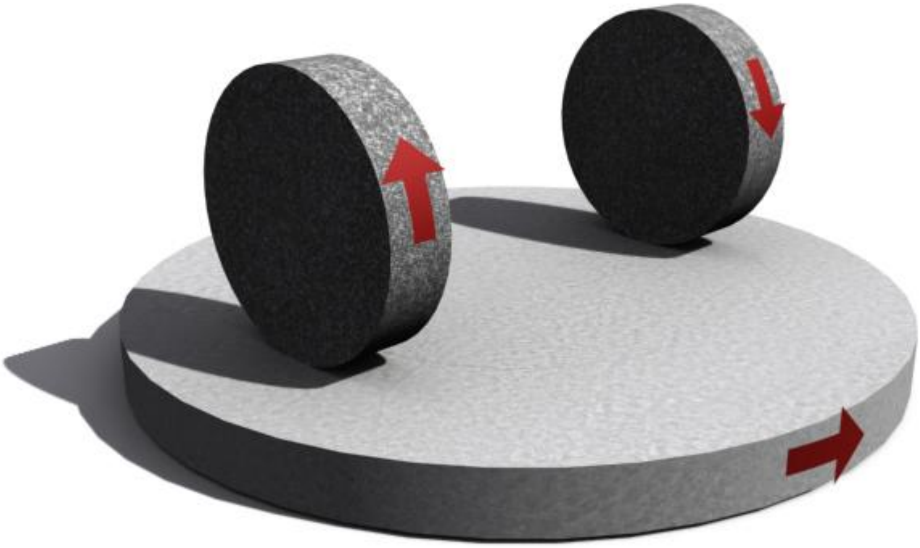

Figure 1.3. A schematic of the Taber Abraser, a macroscale wear tester.

Figure 1.3 displays a typical macro scale wear tester, similar to the commonly used “pin on disk” tester. The smaller cylinders produce a wear track that can later be measured to obtain the wear rate. The standard interpretation of results from most macroscale testing is a simple weight loss measurement with respect to the number of wear cycles.

1.5.2 Contact Profilometry

Profilometry is not so much a wear tester, but rather a wear analyzer. Accurate representation of the surface and surface parameters can be achieved that are paramount in learning about friction and wear at these reduced scales. A surface profile is obtained by mechanically moving the stylus over the sample and recording a certain number of height points of the stylus along its movement [25].

Most contact profilometers commonly provide 2-D views of just the profile, and the wear rate can be analyzed by integrating the wear track to determine total volume loss per number of scans. Significant techniques have been employed in analyzing wear tracks with profilometry ensuring that only the wear area and not certain surface deviations are included in the calculation. Jiang presents a valley seeking method that can be performed in the profilometer data analysis software to ensure that the area being integrated is the actual wear track or scar. This new method finds the outer boundaries of wear scars using the projected area at the edge. It is a valley seeking procedure because the slopes are compared to find where successive slopes are all negative. This new projected area can be integrated to find the area within the boundaries [26].

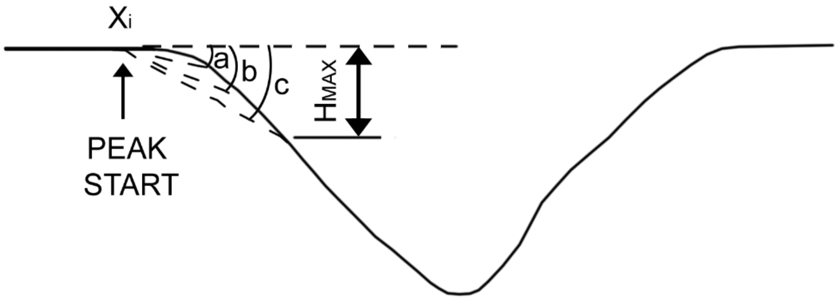

Figure 1.4. A representation of the analysis performed to accurately obtain the limits of the wear scar.

An H_{max} value can be chosen in the analysis software as a critical low point based on the surface roughness and step size between slopes analyzed. This avoids the situation of local asperities or general surface variation causing successively negative slopes and being chosen as the limit of the wear area.

However, optical profilometry has become the new standard in profile measurements, solving the problems of speed, stylus wear, and vibration isolation. Contact profilometry is still the best method in measuring curved surfaces or reflective surfaces that could scatter a laser. Contact profilometry is also suited for sharp ridges in a sample, but physical dimensions (stylus radius) can hinder certain scratch depth analysis. [27, 28].

1.5.3 Scanning Probe Microscopy

Scanning Probe Microscopy (SPM) has revolutionized the field of nanotechnology, as it provides three dimensional quantifiable images of nano structures. SPM imaging is a very popular imaging technique because of its inherent high resolution, ability to work in an ambient air and fluid environments, and the simple sample preparation.

1.5.4 The Atomic Force Microscope

The Atomic Force Microscope is also a recent player in the SPM world, being invented in 1985, it provides significant advantages over other methods, such as scanning tunneling microscopy, which require a conductive sample.

The principle of AFM operation lies in the reflection of a laser beam off the cantilever that supports the tip which is usually made of silicon, silicon nitride or diamond. The laser beam is reflected from the tip, and the angle of reflection changes with the position of the cantilever. The friction between the tip and the surface of the material causes torque that can be measured by the laser beam reflection.

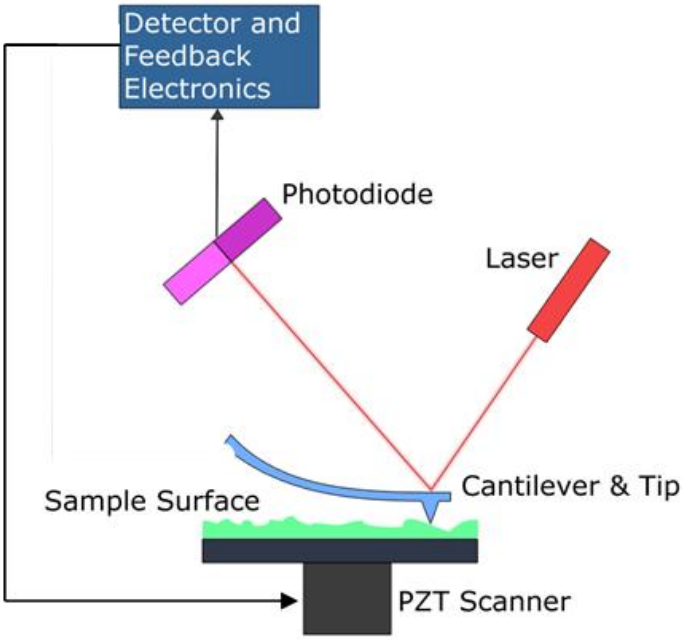

Figure 1.5. A schematic of contact AFM scanning.

Many factors influence the behavior of the tip and the surface; including the environment (humidity) and the sample preparation [29]. Contact mode requires the repulsive force between the tip and the surface to remain constant. The AFM tip is modeled as a perfect sphere making the contact with the sample material single-asperity [1]. Repulsive forces are electrostatic in contact mode [4].

There are disadvantages of using AFM in that it is difficult to get a proper tip geometry calibration, so the data is mostly qualitative. This qualitative nature is also a problem in getting an accurate idea of the force applied to the sample. In an AFM, forces are inferred from the measured deflection of the cantilever, while a nanoindenter performs force controlled measurements. However, when compared to scanning capable nanoindenters, AFM possesses significant advantages – it allows lower loads, and has a better positioning accuracy.

Imaging in AFM is often performed in the tapping mode, especially on biological samples because the contact mode will destroy and remove the delicate molecules [30]. The versatility of the AFM lends it to be applicable to many different kinds of samples and many different testing regimes, including biology and MEMS, however this versatility brings with it complications that need to be addressed to ensure proper data interpretation. One instance of this is tip characterization [4]. A difference in the size of scanning tips is an important parameter, especially in contact mode AFM. Experiments performed on NaCl with a sharp conical tip and a larger blunter tip that contacts about 200 atoms were seen to produce strikingly different results in friction regimes. The sharper tip digs into the surface, and then the temperature is brought to near the melting temperature, the friction levels drop, a phenomenon attributed to “ice skating” where a molten region is formed. The blunt tip merely grazed the surface, but saw an increase in frictional values once the temperature was raised [3]. Without accurate knowledge of tip geometry, the properties of friction and wear can not be thoroughly understood, since they are contact dependent.

1.5.5 The Hysitron Triboindenter

Wear testing on a smaller scale, at the micro and nanometer regimes, requires a thorough understanding of the equipment to separate thermal, feedback, and imaging artifacts from actual physical properties.

The Hysitron Triboindentor is a versatile nanomechanical characterization machine that uses a patented three-plate capacitive transducer which serves as an actuator and sensing element of the machine. The tip that is used for testing is also used in mechanically scanning the surface. This increases the positional accuracy of the experiment by avoiding the need for a transition from optics to testing tip. In terms of stability, the Hysitron nanoindenter actively damps vibrations below 200 Hz using piezoelectric vibration control stages and passively damps those above 200 Hz. The Hysitron tool is enclosed to minimize thermal gradients and passively damp acoustic vibrations, which can significantly affect measurements at such a small scale.

The possibility of thermal drift effects seen when large currents are needed is not a factor with the Hysitron transducer because it is actuated electrostatically. The displacement is measured by a change in capacitance, while the force is being applied. A three plate capacitive transducer is attached to the piezo to provide imaging capabilities. A voltage is applied to the bottom plate of the capacitor, which electrostatically pulls the center plate down. This transducer also monitors the force by using the capacitance sensor of the transducer. This is essentially the “feedback” for system control.

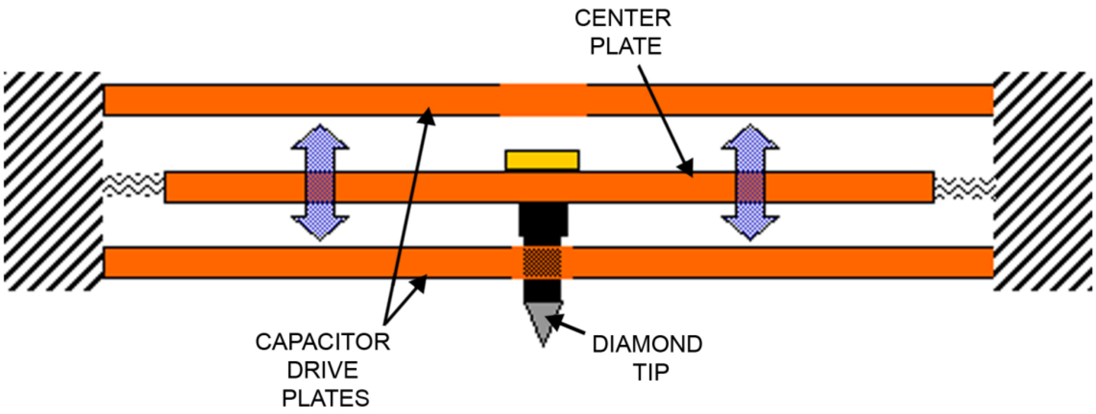

Figure 1.6. A cross-section of the Triboindenter transducer.

The 3 axis piezo scanner also provides the fine scale positioning of the tip (Figure 1.7). The piezoelectric material changes its shape in response to a voltage applied to it. When voltage is applied to one side, it lengthens, which causes the scanner to bend to the side. It is divided into four quadrants that control the +X, -X, +Y, and –Y directions. The large top solid piece controls the +Z and –Z direction.

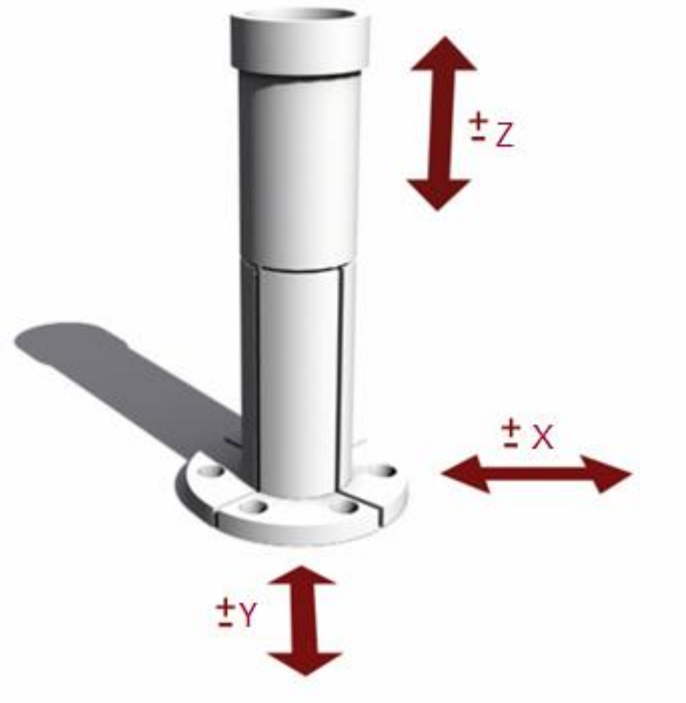

Figure 1.7. The Hysitron piezo scanner. The 4 quadrants for X and Y axis control and upper solid piece for Z movement control are labeled.

However, the piezo is afflicted by negative side effects such as hysterisis and creep. In an ideal world the piezo would deform linearly with respect to the voltage applied. In wear measurements, the piezo is forced to scan topography through hundreds of scans. This constant change in voltage increases the probability that the mechanical response of the scanner will lag behind the voltage applied. Creep becomes a nonlinearity issue when the voltage applied is suddenly and drastically changed. A physical example of the voltage suddenly changing would be a step height on the surface of a sample. If this occurs, the piezo scanner will not be able to retract instantaneously, and will overshoot and the force will possibly "ring" until contact is found again. These issues are usually apparent from looking at the profiles of the scan line while scanning. Large offsets in the scan lines from the forward and reverse scan lines give an indication of hysterisis, and "ringing" can be seen on sharp step heights in the scan lines as well. The tip geometry and partially the feedback loop also produce variations in profile images of the sample depending on which direction scanning is taking place. Figure 1.8 shows a schematic of the tip movement and corresponding profile that would be obtained for the given scan direction over a sample step height. Actual data of profile views can be found in Chapter 2.

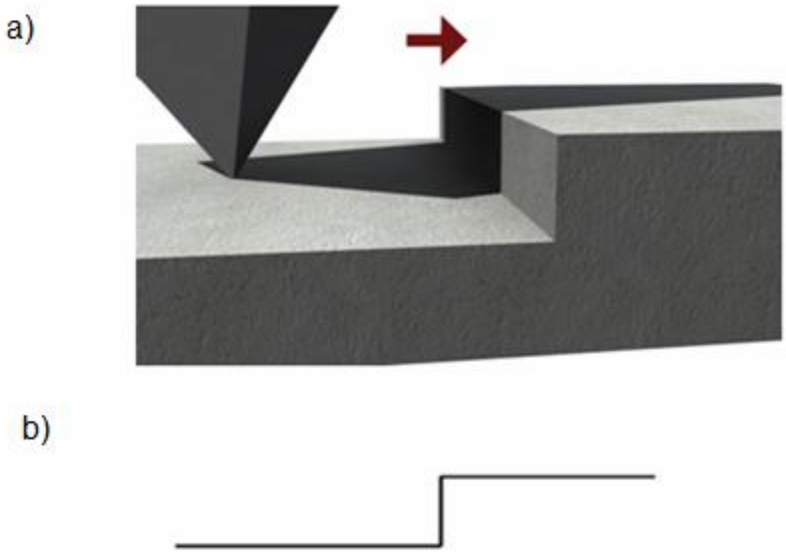

Figure 1.8. The directional dependence of the obtained profile due to the tip geometry. a) a schematic of the tip approaching a step height from the left and b) the corresponding profile view. c) A schematic of the tip approaching a step drop from the right and d) the corresponding less accurate profile.

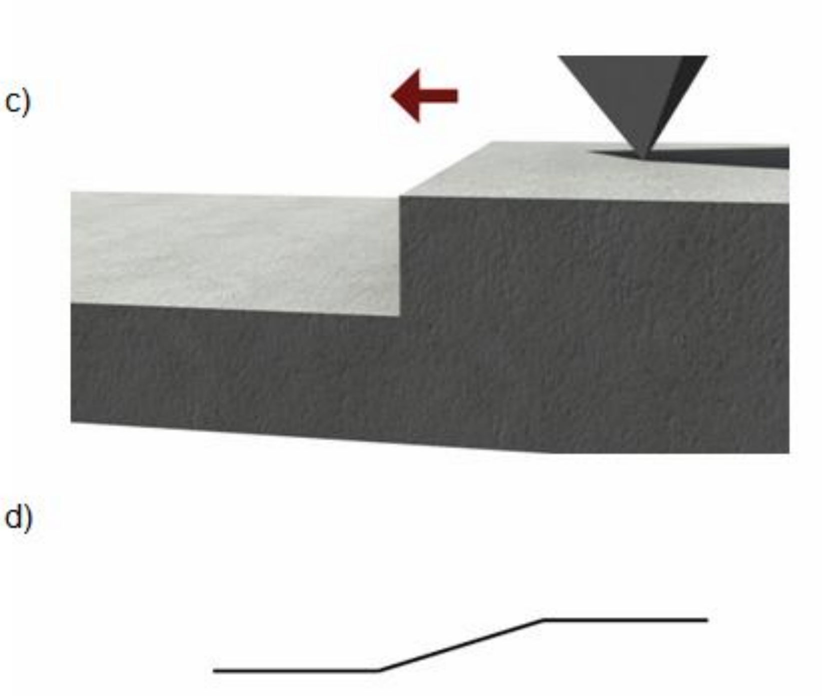

Figure 1.8. (Continued)

The Hysitron operates using an adjustable Proportional, Integral, Derivative (PID) controller that determines how fast the scanner reacts to changes in the sample topography. Appropriate settings are essential because if for example the integral gain is too high, the tip may oscillate, or in the opposite regime, if the integral gain is too low, it will not react quickly enough and wear of the sample can occur when it comes into contact with higher peaks on the sample surface [31].

1.6 Surface Patterning: Ripples

Once scientists and researchers learned how to manipulate materials at the nanoscale, surface patterning and characterization became an exciting field with unlimited texture possibilities. With tiny nanostructures having the possibility of influencing drug delivery, MEMS devices, and countless other facets of technology, this surface manipulation is receiving a lot of interest.

1.6.1 UHV AFM Ripples

It has been shown originally in the ultra-high vacuum (UHV) of 10^{-10} Torr that repeatable scanning of the KBr single crystal (100) surface in an AFM with a silicon nitride tip causes surface reconstruction of wavy patterns forming perpendicular to the tip motion, coinciding with the $\langle 1\,\bar{1}\,0 \rangle$ KBr crystallographic direction. This research was inspired by similar UHV AFM experiments performed on KBr and Al single crystals by another group [31, 33]. In those experiments, the AFM cantilever tip repeatedly moved along a single scan line, which resulted in periodic pile-up structures forming around that scan line. Repeatable square surface imaging results in nanoripples forming perpendicular to the scanning direction. Figure 1.9 shows the InSb sample after 100 scans and a normal load of 34 nN. The distance between ripples was found to correlate with the tip radius. When cleavage steps were present on the sample's surface, they distorted the original perpendicular ripples alignment, but eventually the ripples eroded and became perpendicularly aligned. When these same experiments were reproduced using a regular AFM, outside the vacuum, no ripples could be produced. This may be associated with the fact that UHV-prepared surfaces have higher surface energies than surfaces with adsorbed species in ambient environment. Our research has made an attempt to produce these ripples both in the Hysitron and AFM in the ambient environment.

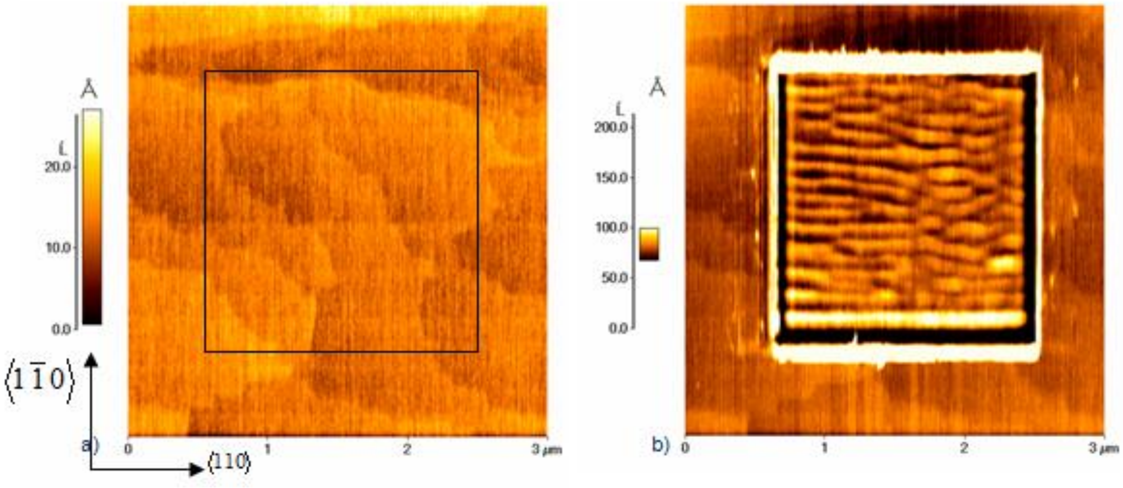

Figure 1.9. a) Contact mode AFM image of InSb surface obtained in ultrahigh vacuum. Square outlines the scan area; b) The same area after 100 repeated vertical scans in ultrahigh vacuum [30].

1.6.2 Similarities in Nature

Ripple pattern can be observed at the macroscale in nature in instances like sand dunes, ocean floors, cumulus clouds, and even the surface of Mars.

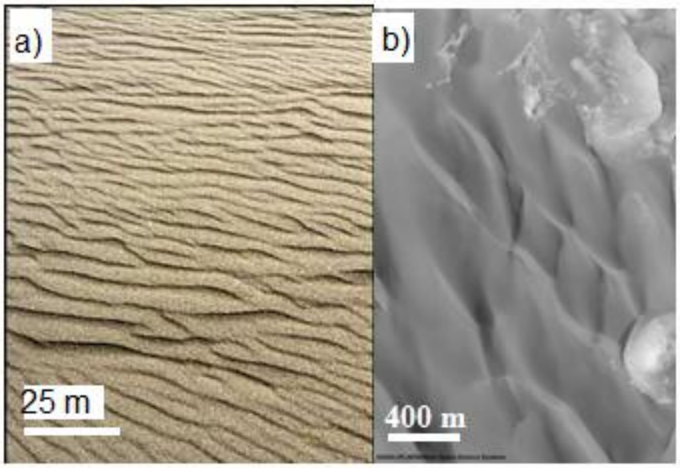

Figure 1.10. Macroscale ripples in nature. a) Example of sand dune ripples and b) 100 m high ripples on the surface of Mars.

The sediment movement on the ocean floor and cross beds formed by high velocity wind in sand form the familiar ripple pattern at the macroscale. Sand dune ripples are formed when the wind tries to pick up loose sediment but only carries them a short distance before they begin to pile up on each other forming ripples perpendicular to the fluid flow as observed in the nanoscale ripples as well. The wind velocity increases in the low points, having enough energy to pick up more sand particles, and slows down over the steep incline of a ripple, and drops some particles, thus increasing the wavelength of the ripples and self propagating the pattern [34].

1.6.3 Ion Beam Ripples

Focused electron and ion beams can cause surface reconstruction and form ripples, which periodicity depends on the incidence angle, the beam energy, and residence time [35]. Experiments where an ion beam was blasted at a glass surface produced ripple patterns at the nanoscale. These ripples formed perpendicular to the beam of ions that bombarded the surface except when defects in the glass were encountered, and the ripples oriented parallel to the defect [36].

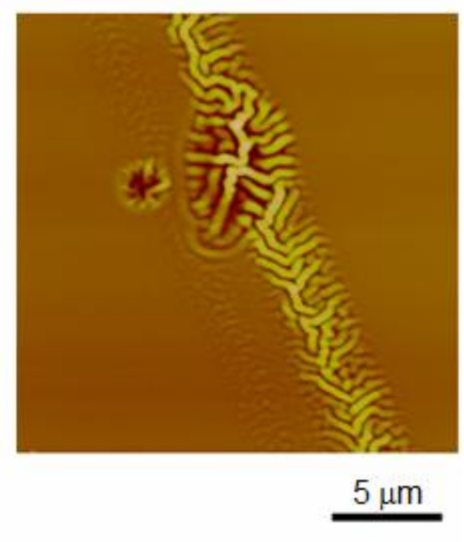

Figure 1.11. Example of ripples caused by a focused electron beam [37]. 200 nm Z range.

1.6.4 Polymer Ripples

Another instance of ripples produced in the AFM has been achieved in thin polymer films [35]. Ripples formed perpendicular to the scanning tool direction and were 10-100 nm in wavelength. Polystyrene was scanned at the normal load of 17 µN, and the ripples formed were aggregate groups of polystyrene molecules. Over time with continuous scanning of the surface, the size of the ripples, or “bundles” grew in size. The ripples formed oriented themselves perpendicular to the tool tip direction, even if the sample was rotated after the surface had produced ripples in a certain direction. Experimenting with ranging molecular weights of polystyrene produced no change in the 12 µm square ripple pattern in terms of the wavelength and pattern structure.

1.6.5 Coelctrodeposition Ripples

Experiments with coelectrodeposition using a solution of Ag and Sb resulted in light and dark patterns formed on the electrode [36]. The ripple patterns formed were very similar to the patterns observed on KBr and InSb samples during wear experiments and large scale ripple patterns on sand dunes and ocean floors. When the element distribution throughout the pattern was expounded, the crystals making up the pattern were strikingly segregated within the patterns; the lighter portions were rich in Ag, while the darker patterns contained more Sb, and O. The propagation of the ripple patterns is suggested to be due to convection, where the flow is driven by buoyancy differences within the ions. Other physical factors might be at work in the propagation of these ripples. Periodic patterns are also commonly observed in fracture of thin films and multilayers, both in tension and compression [37].

1.7 Environmental Effects in Wear Testing

Research in material behavior in varying environments, especially lubrication performance, is a constantly expanding field, particularly with the growth of the thin film industry. The performance of thin films in the presence of friction in many different environments is vital for their reliability. At the macroscale, most wear testing preformed in the presence of fluids centers around engine cooling and refrigerant viscosity. These macroscale tests are important because the best lubrication that in return yields the least wear and friction means better fuel economy, which in today's world is a goal every manufacturer is striving to achieve [38]. Most surfaces are covered by a few molecules of other substances attracted to the surface. Water is a common molecule on the surface of materials because of its sheer abundance in the ambient environment, and its ability to condensate [39]. The wear experiments carried out in the presence of water were all performed on gold samples, a highly researched material not restricted to technological applications like electrical connections, but also having great importance in the dental industry as well [40]. As dental technology and hygiene has increased over the past 100 years, people are much more likely to have their original teeth for a longer period of time. In this situation, tooth wear and degradation becomes an issue, and studies of natural tooth enamel materials, gold, and other restorative materials are important [41].

Wear testing of gold in varying environments has important implications since gold is widely used for its resistance to corrosion more so than its conductivity. Wear testing in water adds another degree of complexity, as the wear mechanism can evolve differently, as was seen on polymer wear tests by Prehn [42]. Polyetheretherketone (PEEK) matrix polymer composites showed abrasive wear in a dry environment, while erosive wear was present in water wear experiments. A changing wear mechanism is not just a phenomenon attributed to polymers, but is also observed in steel, aluminum and other metals [42].

PVD sputtered gold approximately 150 nm thick on (100) silicon substrate was tested by using a microtribometer for its frictional values. Tested at loads of 1-20 mN, using a steel cantilever of 169 N/m stiffness at a relative humidity of 33 and 84%, the coefficient of friction of gold was not found to change from 0.2. This was attributed to gold being a hydrophilic material, which already reached its saturation point. The authors summarized that capillary forces develop when a material is saturated increasing the frictional values [41]. Mica, a common substrate material that is also extremely hydrophilic, has been seen to exhibit a strong dependence of frictional values on humidity [14]. Experiments performed on NaCl showed a distinct increase in frictional values above 45% humidity in contact AFM scanning. It was concluded that a water surface monolayer was essential for increasing the frictional values [43].

The pH of a liquid has been shown to have a linear relationship with frictional values at the nanometer scale as well, where increasing pH levels lowers the lateral force observed. Silicon was tested in a fluid cell AFM with NaCl with varying levels of HCl to adjust the pH, and scanned over a single scan line. The lateral force was found to be independent of velocity, showing that the driving force was frictional as opposed to viscous [45].

A model of the kinetic frictional force used an equation from Isrealivhvili in describing a frictional force in the silicon pH experiments :

$$F= C_1A+C_2P \tag{8}$$

where C_1 is the mutual adhesion of the two surfaces, A is the adhesion hysterisis or energy dissipated, C_2 is the surface roughness and P is the applied load [45].

1.8 Scratch Testing

Abrasive wear resistance generally correlates with a material's hardness so the hardness test became commonplace for evaluating a material's abrasive wear resistance. However, this correlation was found not to hold true for thin coatings [46]. Additionally, many common wheel based wear testers are too severe for coatings. Scratch testing can provide a better evaluation of abrasive resistance of a material that is deposited as a thin coating. In many small scale applications, a thin gold film is used as an interconnect for electrical devices, therefore a scratch test can be a valuable experiment in evaluating gold wear properties. Technology continually strives to achieve smaller and smaller products, and this pushes coating thickness to smaller and smaller values. However, these coatings are still expected to provide the same tribological performance [47]. Much of scratch testing is devoted to providing information about a coating's practical adhesion, but wear resistance is equally significant [48].

In terms of quantifying a material's scratch resistance, several definitions have been proposed, such as dynamic hardness, tangential hardness, and specific grooving energy. More recently an ASTM scratch standard was produced; however problems still lie in the reproducibility and definitions of those terms [49]. To apply the definitions for scratch hardness, most often the contact area needs to be calculated, a difficult task if working with a material that can viscoelastically recover a large percentage upon unloading [50].

A scratch test is most often performed by a diamond tip scratching along the surface with a constant normal load. The depth of scratch is then analyzed to provide information about the material's scratch resistance. Another method useful in very thin coatings (approximately 5 nm or thinner) is to constantly ramp up the normal load until breakdown of the coating occurs. This method is beneficial when instrument resolution becomes a factor in measuring scratches 5 nm or less in depth. When the coating is penetrated, that load is defined as the critical load [51-53]. The critical load is determined through the frictional force. When the frictional force becomes irregular, it is attributed to breakdown of the coating. This method is fairly reliable, but more recent methods involve using a conductive carbide blade to measure the contact electric resistance (CER) at the cutting point. When this value is zero, if the tip scratches through to a conductive material below, it corresponds to the critical load of the coating. Scratch testing with the ramped normal load method becomes complicated because the underlay or substrate can be a significant factor in the coating's scratch resistance. The deeper the scratch, the more the properties of the substrate influences the scratch resistance. This composite interaction is always measured during scratch testing using ramp loading because the scratch goes to the point of breakdown, involving the underlay [43].

It is generally accepted that much of scratch frictional forces come from a combination of ploughing and adhesive components. For reciprocating scratch test, it has been shown that the plastic ploughing component wanes off, leaving the majority of frictional force due to adhesive friction until coating delamination [54].

Not only can coating adhesion and wear resistance information be obtained from the scratch test, but information about the critical plastic strain resistance can also be gained [55]. It has been difficult to experimentally determine a strain to failure value, because the strain fields in a wear situation are different from those in conventional tests like tensile, compressive and torsion. Using an acoustic emission (AE) sensor, the point of microfracture during the scratch can be obtained correlating this moment to the maximum plastic strain the material can withstand.

1.9 Objectives

This research was aimed to study the rippling of materials at the micro and nanoscale, and additionally replicating this rippling outside of the UHV environment. Special interest was paid to varying environmental conditions and observing the effect on wear and pattern formation. Varying testing equipment and utilizing different testing methods was also performed to obtain conclusive correlations of material’s response to wear testing in varying forms.

This introduction has reviewed the basics of wear and friction, including some relevant issues like adhesion and stick slip friction. Observations of small scale patterning in other areas of research have been discussed, as well as humidity effects on nanoscale wear testing. Careful attention has been paid to the variety of different wear testing methods and their relevant issues relating to small scale materials.

CHAPTER 2

NANOSCALE PATTERN FORMATION

2.1 Introduction

Due to the inherently complex and constantly changing nature of the wear process, a standardization of testing does not exist. In the following experiments, different wear testing techniques were employed to gain an understanding of the material's behavior under such conditions. A relatively common microscale wear test technique is creating a "wear area" (Figure 2.1). This square indentation is where the tip scanned the surface of KBr under a constant normal load. This technique is useful in acquiring information on wear over an area, and tests are relatively simple to set up in a raster scanning machine. Images can also be taken after and during scans, so progressive wear information can be obtained.

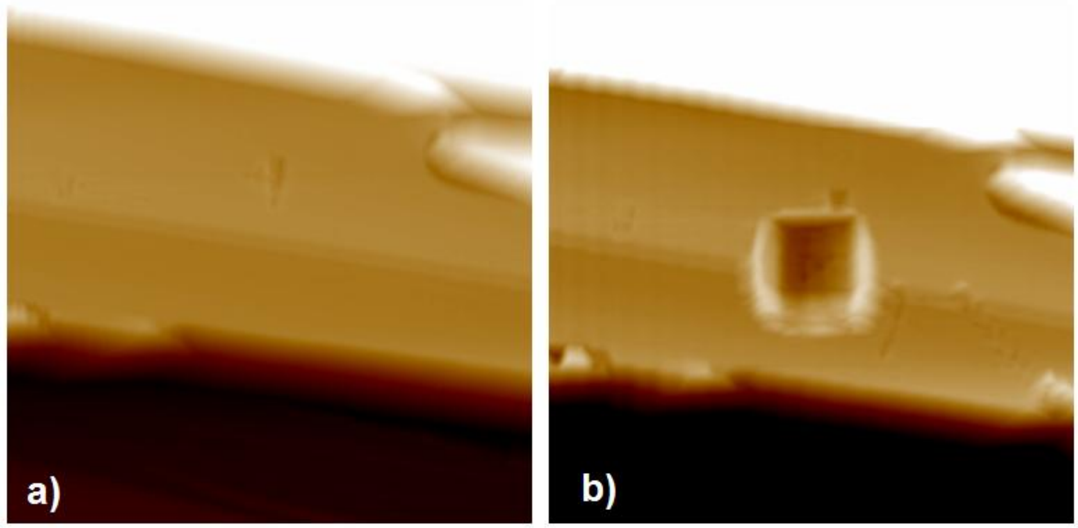

Figure 2.1. a) KBr sample surface before a wear test b) After 10 scans at 2 μN normal load a wear trench is formed. Z scale is 300 nm.

Initial experiments were performed on KBr single crystal, a transparent ionic solid. This material was chosen to reproduce experiments performed in the Ultra High Vacuum Atomic Force Microscope (UHV AFM), where KBr was seen to ripple during scanning (Figure 1.9) [30]. The goal of these experiments was to bring observed results seen in the UHV system out of the vacuum and into the ambient environment using the Hysitron Triboindenter. Single scan line pile up ripples were replicated outside of the vacuum and studied as well [8]. Insights into nanoscale patterning phenomenon is extremely valuable especially as technology pushes into the small scale regime. It is of interest to study these ripples and their formation because of their relevance to the growing field of research in surface patterning.

2.2 Experimental Details

Subsequent experiments reproduced the rippling effect in ambient laboratory atmosphere using the Hysitron Triboindenter. The tool is capable of repeated surface scanning, producing AFM-like images. It can scan up to 80x80 μm^2, making 256 passes of an area with a rigidly supported diamond tip. Scanning experiments were performed with a normal load of 2 μN on freshly-cleaved KBr single crystal surfaces with a Berkovich diamond tip of 100 nm tip radius in an ambient lab environment. This experiment produced ripples after 20 scans of the 10x10 μm^2 area (Figure 2.2). The ripples formed perpendicular to the tip motion direction, as observed in the UHV AFM ripples as well.

Single scan line experiments were performed on KBr in the ambient environment using a Park Scientific AFM with a silicon nitride tip with a 10 nm radius. The scans were performed in contact mode and scan parameters such as normal load, scan speed and length of scan were varied. Results of the scanning produced a ripple pattern in the pileup structures of the scan line. These were inspired by other tests preformed in the UHV AFM [8]. In those experiments the ripples grew in width correlating to an increase in normal load. Additionally, the environment in which the KBr was cleaved was found to significantly affect the morphology of the resultant ripples. KBr cleaved in the vacuum produced narrower ripples than the KBr cleaved in ambient conditions then moved to the vacuum for scratching. This environmental dependence elucidates the significance of reproducing the single scan line ripples in the ambient environment for experimental significance.

2.3 Pattern Formation Results

2.3.1 Potassium Bromide Rippling

Figure 2.2a is the original cleaved KBr single crystal surface, and Figure 2.2b presents nanoripples formed after 20 scans of the area in Figure 2.2a. In comparing Figure 2.2a and 2.2b, the initial cleavage steps in the KBr sample can be seen very sharply in Figure 2.2a, and then eroded in Figure 2.2b. These results parallel the UHV AFM experiments on KBr where cleavage steps were worn down during the scanning experiments. A movie constructed of single image scans of KBr single crystal reconstruction due to scanning at 1 Hz can be seen online [42]. The scan size is 4x4 μm^2 which is the area the tip scans over; the effective area that is wear tested. A topographic image of a rippled KBr surface can be seen in Figure 2.3a. The subsequent profile (Figure 2.3b) displays the height and width of the ripples.

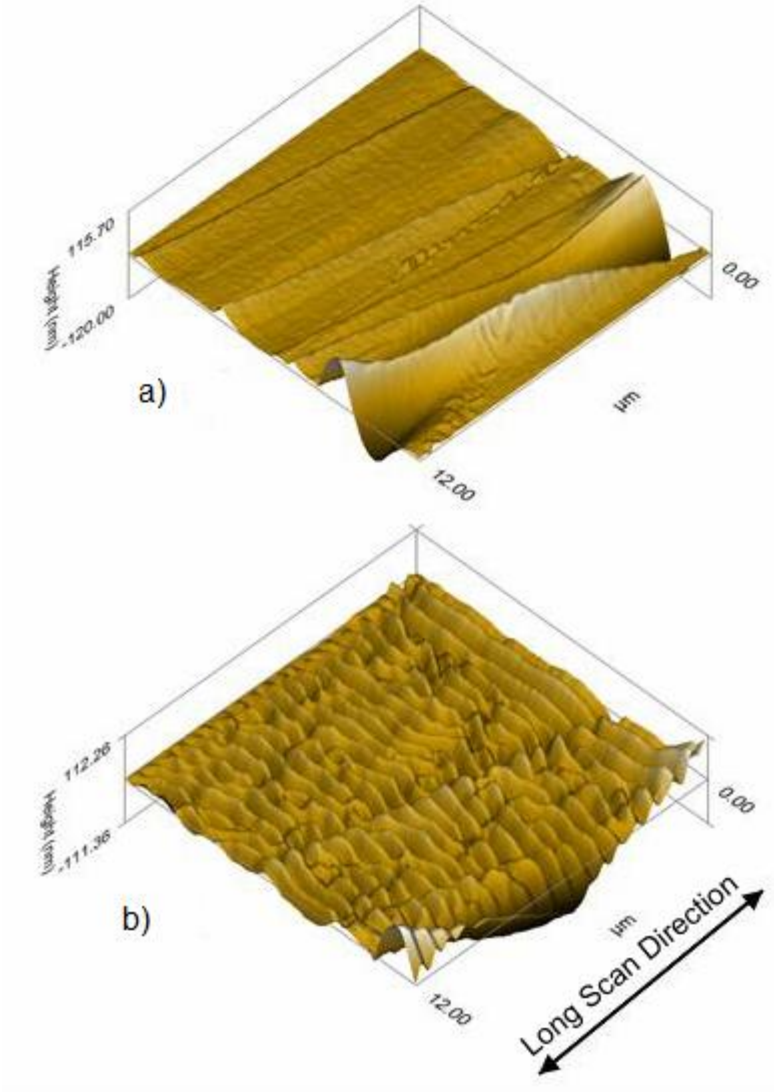

Figure 2.2. a) Original KBr single crystal topography surface image showing scratches and cleavage steps; b) the same surface after 20 scans with a Berkovich diamond tip (100 nm tip radius) with a 2 μN normal force. The arrow shows the scanning direction.

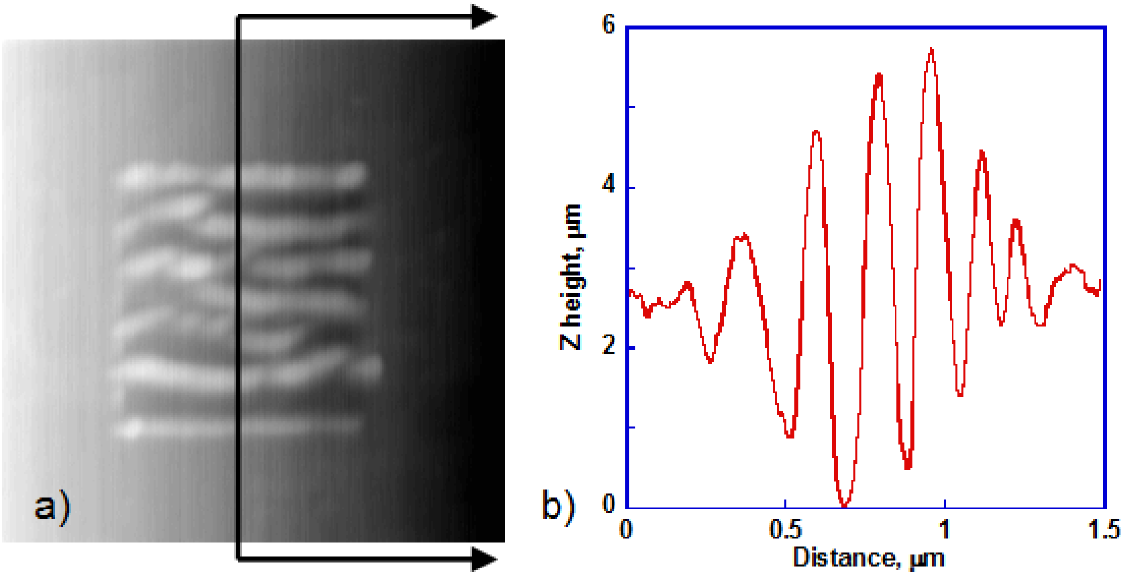

Figure 2.3. a) Shows a 1.5 square μm scan of KBr displaying the 1 μm square wear area after it had been scanned; b) topographical vertical cross-section of a). Courtesy of Bartosch Such, Jagiellonian University, Krakow Poland.

Ripples initiate at cleavage steps, and Figure 2.4 is an example of this. The lines are drawn to show where the cleavage steps are located, and how they correspond with the initiation of the ripple pattern. Original cleavage steps (2.4a) were located by inverting the image color, then transferring the pattern to Figure 2.4b.

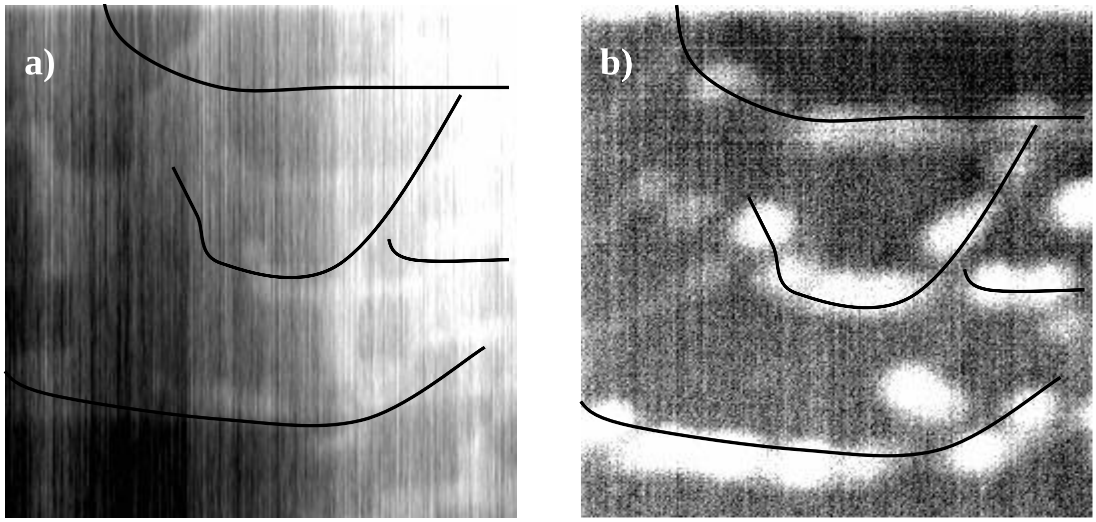

Figure 2.4. a) UHV AFM image of 1x1 μm^2 original KBr surface after one scan at 8Hz; b) the same area after 10 scans at 8Hz. The black lines highlight the crystal steps that serve as ripple initiation sites.

2.3.2 Single Crystal Aluminum Rippling

Single crystal aluminum was found to produce the rippled surface pattern when scanned in the Hysitron. Initiation of ripples took significantly more scans than in the KBr experiments. Sample preparation of the Al crystal was polishing, however the oxide layer was intact during testing.

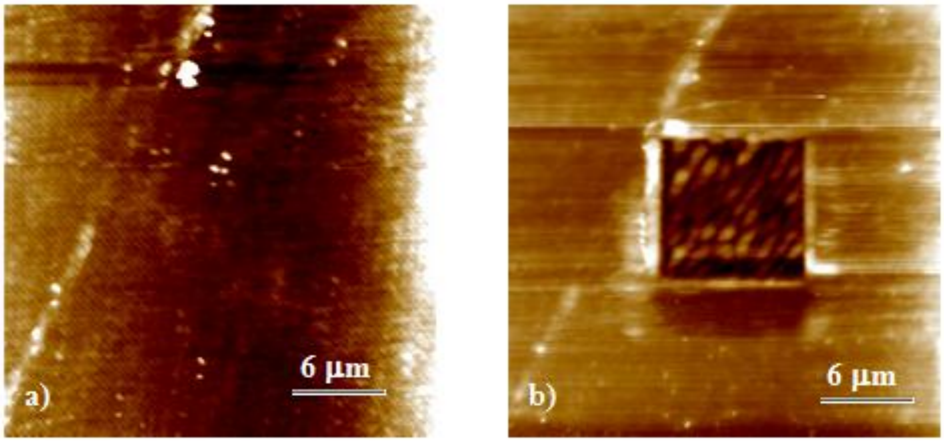

Figure 2.5. a) Topography of Al single crystal before wear and b) nanoripples formed after 1000 scans. Z scale is 650 nm

The ripples in Figure 2.5b are oriented diagonally from the scanning direction, a feature also occasionally observed in KBr where surface features initially influence the ripple's direction, but further scanning orients them perpendicular to the scanning direction. Profile analysis of the Al ripples can be seen in Figure 2.6. Comparing the relative ripple height, KBr ripples are much larger on the order of 2 µm where Al ripple height is closer to 20 nm.

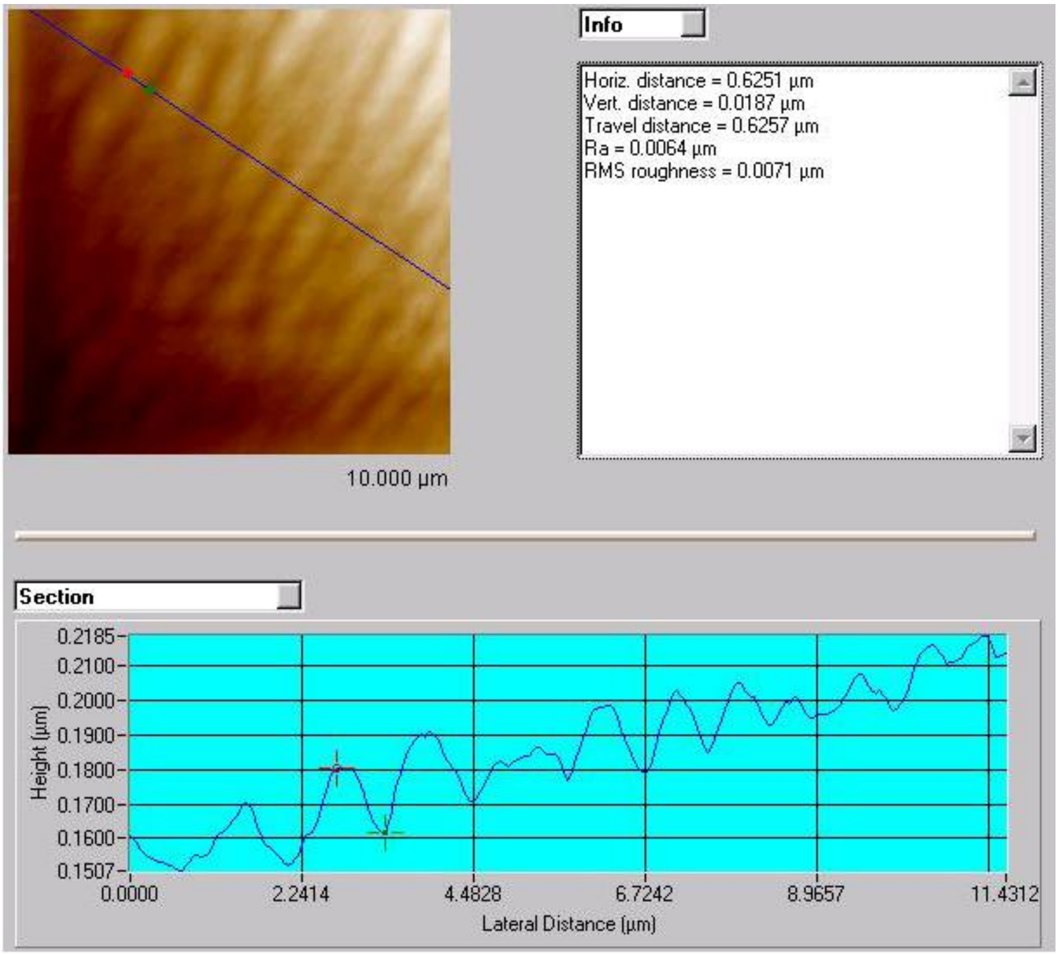

Horiz. distance = 0.6251 µm
Vert. distance = 0.0187 µm
Travel distance = 0.6257 µm
Ra = 0.0064 µm
RMS roughness = 0.0071 µm

Figure 2.6. Analysis of Al rippled area showing an average ripple height of approximately 20 nm.

2.3.3 Gold Ripples

Until the appearance of wear ripples forming on gold, the ripples had only been observed on single crystal materials. This led to a theory that dislocations within the crystal are a possible cause of these structures. However, in testing of sputtered gold and single crystal gold samples in the presence of water on the Hysitron and AFM, the similar rippled surface pattern appeared (Figure 2.7).

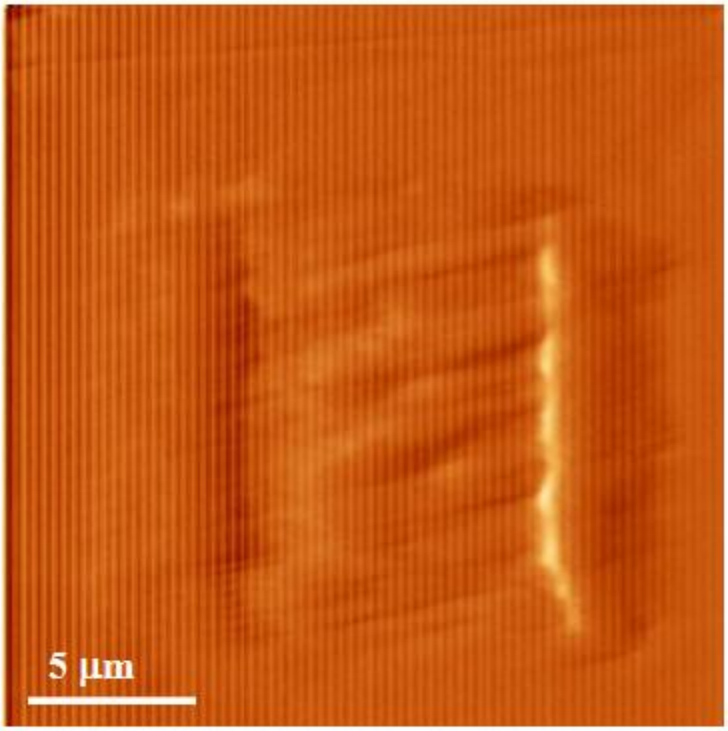

Figure 2.7. Final image after 40 scans showing developed ripples scanned in the Hysitron.

Single crystal gold experiments performed in the presence of water on the Hysitron initially produced common, “normal” wear areas with no pattern formation as can be seen in Figure 2.8. Scanning parameters were 10 µN normal load and 2 Hz scan speed over a 10x10 μm^2 area for 25 scans.

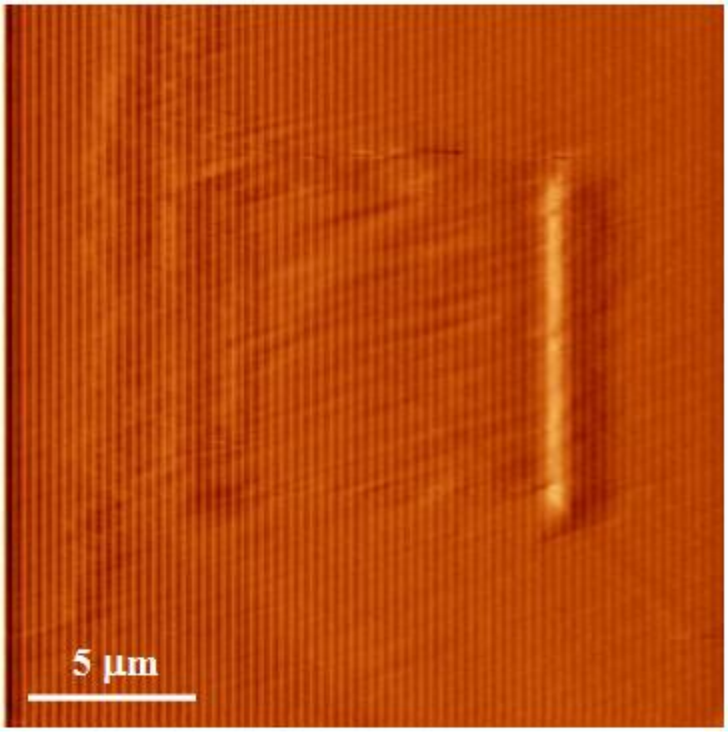

Figure 2.8. 20x20 µm^2 single crystal gold surface - gradient (error signal image) is shown for clarity.

Continuing to scan the images shows the topography variations in the gold turn into ripple initiation sites as scanning progresses. Figure 2.9 was scanned at the same parameters as Figure 2.8.

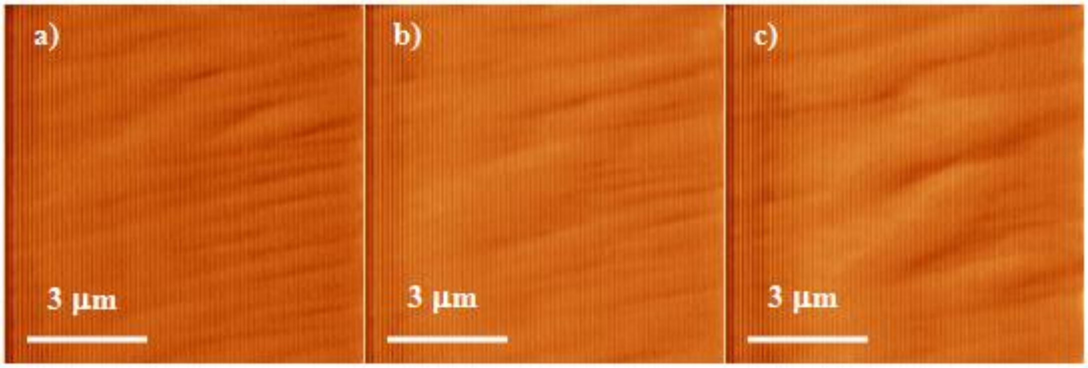

Figure 2.9. Ripple progression on single crystal gold after a) 27 b) 30 and c) 36 scans. Long scanning direction was horizontal.

After zooming out the scan size to obtain Figure 2.7, returning to scan the same 10x10 μm^2 area initially deteriorated the ripples slightly, (Figure 2.10a) possibly due to the tip slight offset when returning to scan the same area. As precise as an AFM is on such a small scale there is still a small degree of position variation, and this offset could disrupt the ripple propagation. The deterioration was not permanent because 5 scans later (Figure 2.10b), the ripples began to form again.

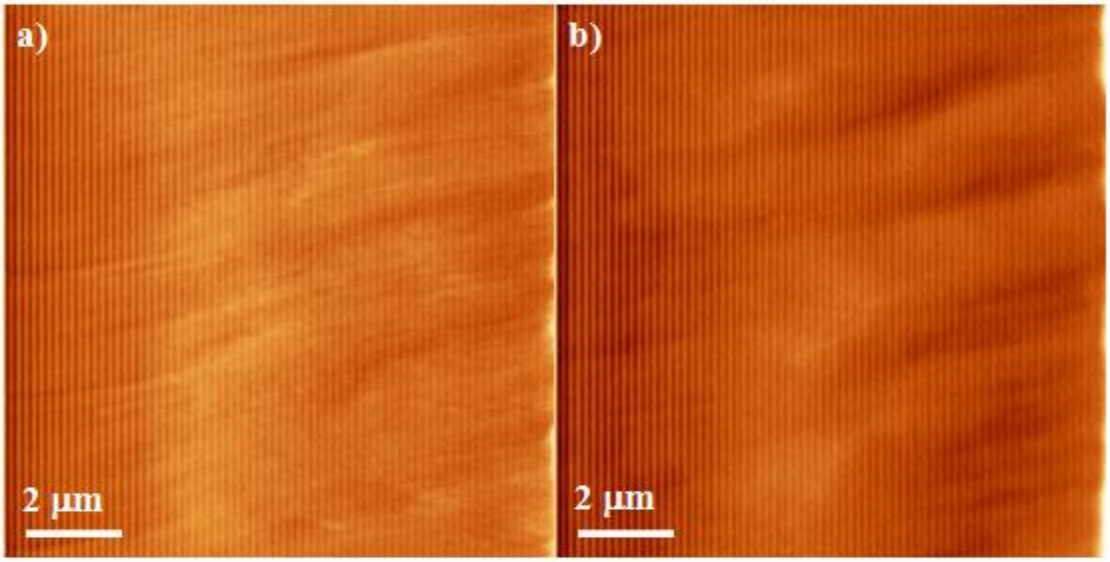

Figure 2.10. a) Scans showing the deterioration (smoothing) of ripples formed in Figure 2.10 b) 5 scans later the ripples form again.

Unlike the KBr ripples, the single crystal gold ripples formed parallel to the scan direction. Tests performed on 3 μm sputtered gold in water on the Hysitron formed ripples perpendicular to the scan direction (Figure 2.11). The sample substrate was silicon and the thickness of the gold was determined through profilometry scans.

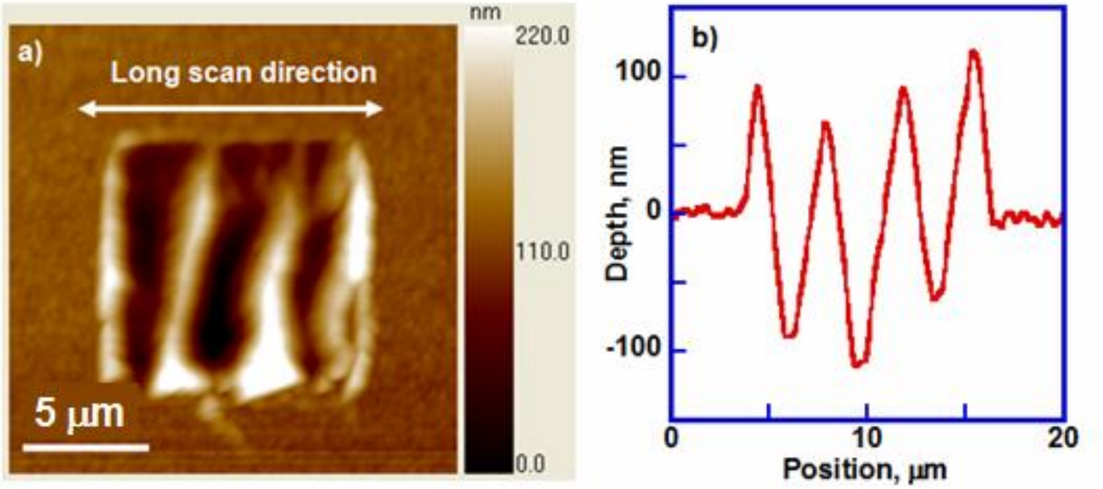

Figure 2.11. a) Wear pattern and b) Wear track of a gold film after 200 wear cycles at 10 μN normal load with a sharp Berkovich tip in water showing surface ripples.

Not only were the ripples formed on the 3 μm gold on the Hysitron, they also appeared while testing in the AFM as well. Figure 2.12 shows the ripples that appeared in the ambient environment in the AFM after only 30 scans of the 3 μm sputtered gold surface. The ripples are also aligned perpendicular to the long scan direction.

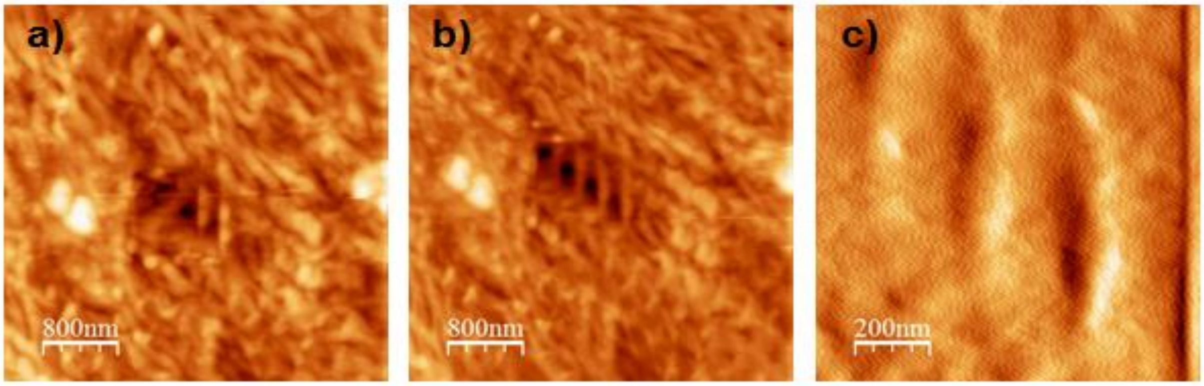

Figure 2.12. Sputtered gold, 2 μN normal load, ambient conditions: a) after 30 scans; b) after 50 scans; c) after 50 scans, 1x1 μm^2 AFM deflection image.

2.3.4 Single Scan Line Rippling

In single scan line testing, where the tip is scanned repeatedly over the same line, Socoliuc et. al. observed rippling in the pile up structures of KBr (Figure 2.13) while testing in a UHV AFM. The Socoliuc results were reproduced in an ambient environment using an AFM with a silicon nitride tip at normal load of 250 nN (Figure 2.14).

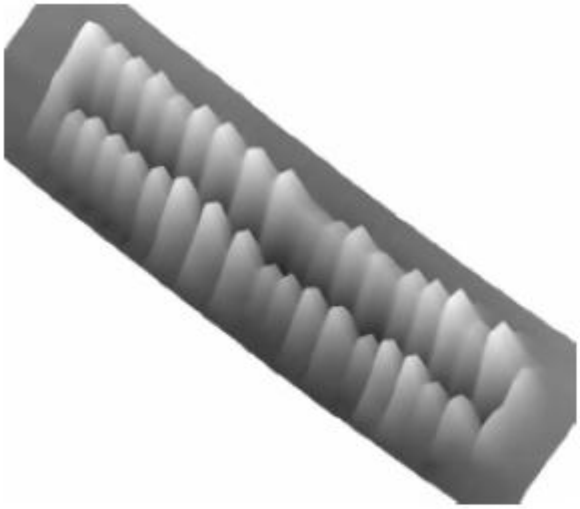

Figure 2.13. Topography image of a 1 μm long groove formed on KBr (001) after 512 scans along the <100> direction, 26.2 nN. Reproduced with permission from Phys. Rev. B [8].

The cleavage steps on the KBr sample did not serve to disrupt the ripple formation as can be seen in Figure 2.14. The line was scanned at 250 nN normal load over a 2 μm scan line at a speed of 7 Hz. The line in Figure 2.14 was scanned for 6720 passes. The higher normal load (250 nN compared to Socoliuc normal load of 26.2 nN) was necessary to induce ripples, experiments at lower loads did not produce the ripple pattern.

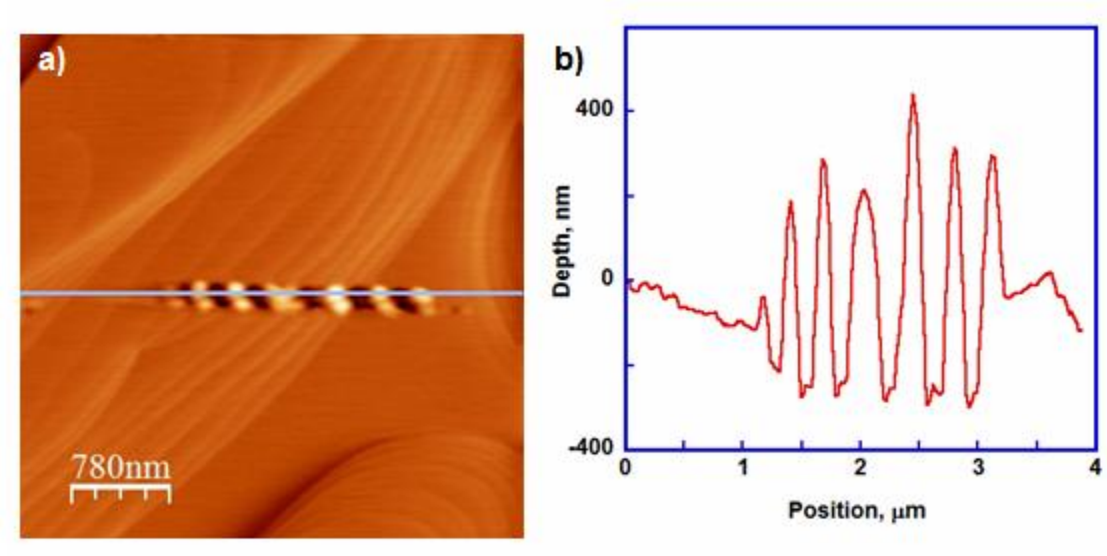

Figure 2.14. Single scan line rippling of KBr in the ambient AFM. The error signal image is often shown because it appears cleaner and easier to observe the surface ripples than the topography image.

Not all single scan line experiments on KBr produced the pile up ripples. Figures 2.15 and 2.16 show experiments where varying the integral gain parameter affected the formation of ripples. Keeping all other parameters the same as those before (normal load, number of passes, speed, scan size), but varying how closely the tip tracks the surface, produced drastically different results. Below a gain of 0.3, no significant ripple structures formed (Figure 2.15, 2.16).

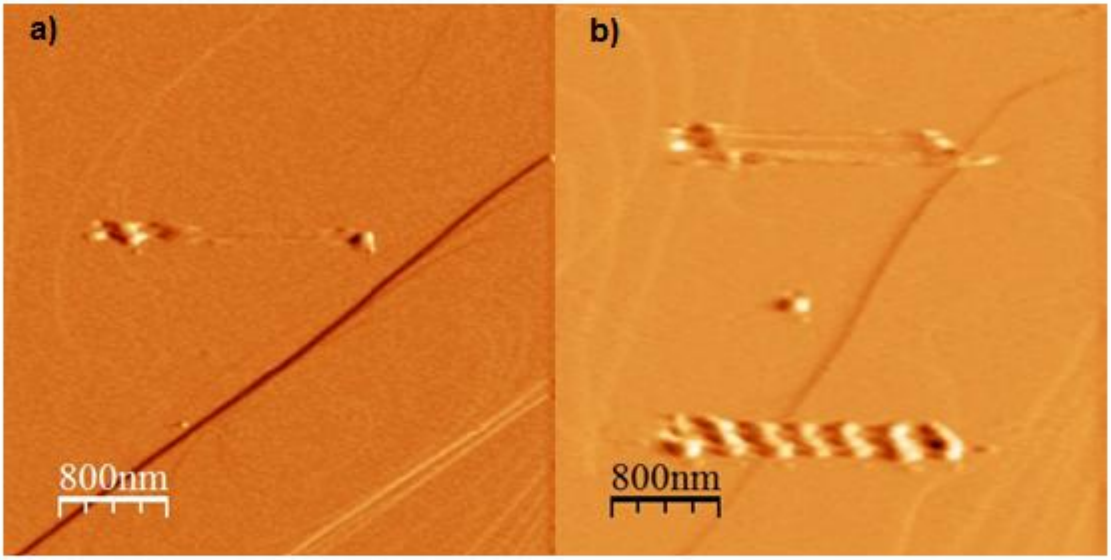

Figure 2.15. a) Scan line taken at a gain of 0.1. b) The top line was scanned at a gain of 0.1 and the bottom scanned at 0.3.

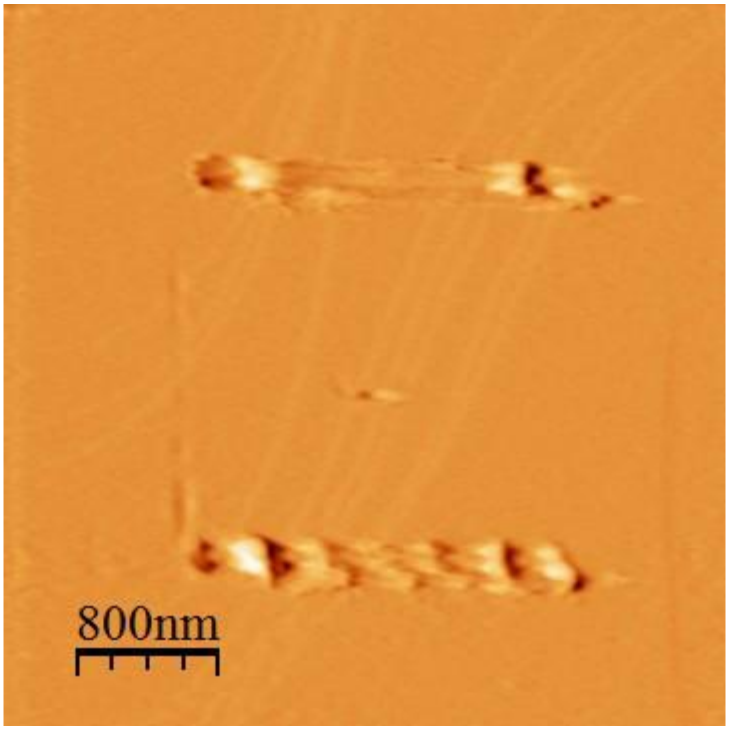

Figure 2.16. The top line was scanned at a gain of 0.2, and the bottom scan was taken at a gain of 0.3.

Several experiments with the gain setting at or above 0.3 consistently produced the pile up structures (Figure 2.17). These experiments were performed at a normal load of 500 nN and 7 Hz scanning frequency. No ripple patterns were produced at lower gain settings, even when the experiment was carried out for a larger number of scans.

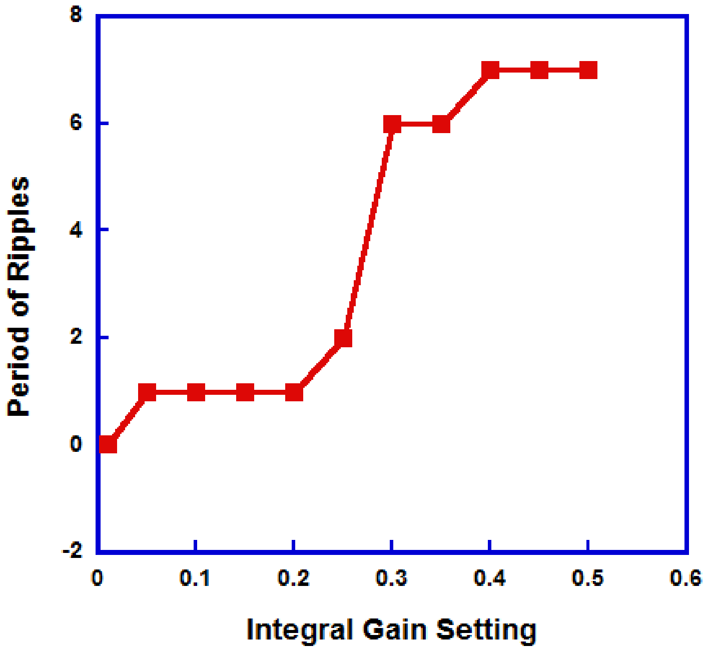

Figure 2.17. Relationship between the number of ripples formed in the pile up structure and the integral gain setting. An apparent threshold to ripple formation occurs at around 0.3 gain.

The gain dependency of ripple formation was not a factor if the normal load was increased significantly. In testing at 2 μN normal load over a 3 μm scan line, the tip dug into the sample producing ripples in the trench; where the tip scans, but not in the pile up structures, where the material is plastically displaced (Figure 2.18). The sample was tested for the same number of scans (6720) as the previous experiments.

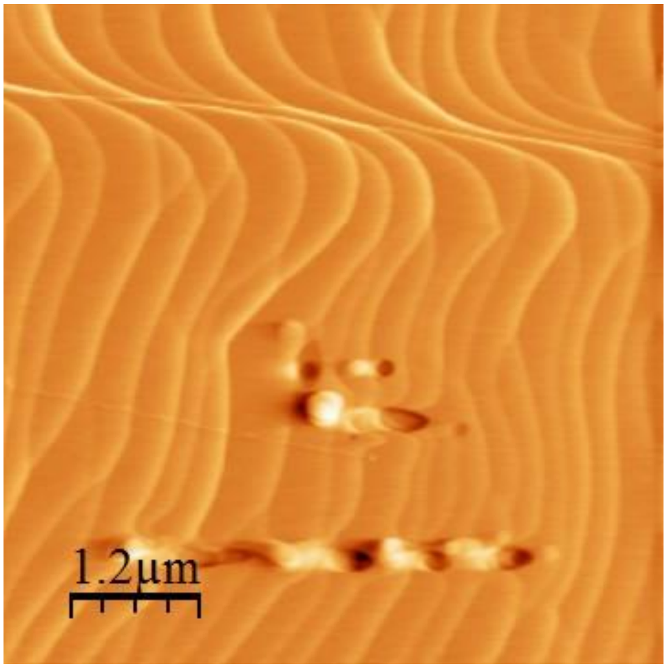

Figure 2.18. KBr sample tested at 2 µN normal load showing the ripples formed in the trench. The sample damage in the center of the image is due to the initial tip placement when it finds contact with the sample.

2.4 Ripples Analysis and Discussion

2.4.1 Slope Effect on Ripple Formation

Another interesting property of the ripples is their tendency to form at the bottom of a horizontal slope. If there is a topographical slope to the surface area, the lowest point in that area is where the ripples will initially propagate from, as can be seen in Figure 2.19 and Figure 2.20. This "slope dependence" has also been seen in rippling experiments performed in the UHV AFM, indicating that this effect is not seen solely in one environment, but is a function of the ripples formation [30]. When the tip encounters a sloped surface, the piezo can not react instantly to the topographical change, and is subject to acceleration down the slope, and then a quick deceleration when encountering the specified edge of the image, and is forced to travel back up the slope. This response time in the piezo could cause a "digging in" of the tool tip into the sample when it is quickly decelerated at the bottom of the slope.

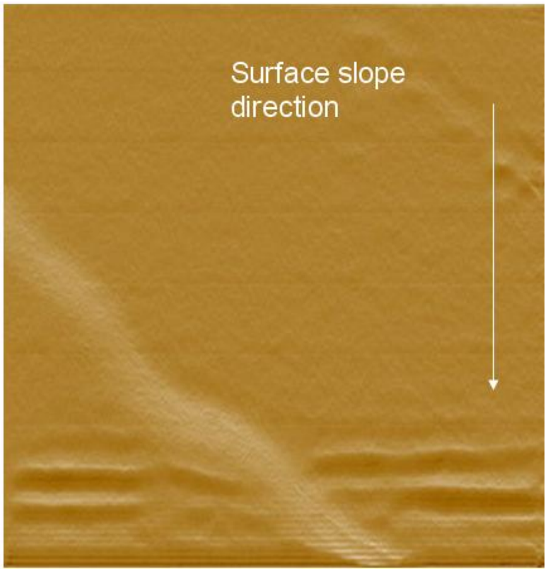

Figure 2.19. KBr early ripple propagation after 10 scans using Hysitron Triboindenter. The arrows indicated the direction of scanning

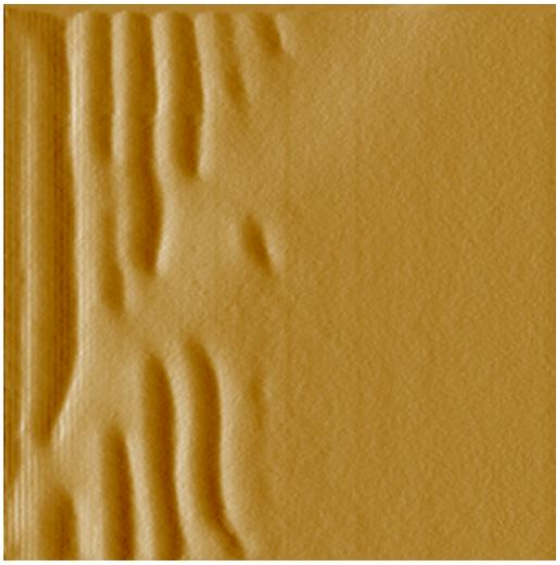

Figure 2.20. A 300 nm tilt over 12 μm showing the ripple patter propagation at the bottom slope of the sample.

2.4.2 Piezo Hysteresis

Piezo hysteresis can cause a phase shift that would be seen in the tool tip movement. This movement is an elliptical path that would drive the tool into the sample deeper on the retraction of the elliptical shape. This difference in depth of the tool tip is a difference in energy required to move the tip. In this way the vibrations are sustained through the periodicity of the force in the tip motion over the surface [47]. In addition, piezo vertical motion time response is different, as it is easier to extend the piezo than to retract it. Both UHV AFM and Hysitron TriboIndenter produced similar qualitative results. AFM has a compliant cantilever, whereas a rigid diamond tip is used in the nanoindenter, although both instruments employ open feedback piezo for scanning.

To further study the piezo effects in the Hysitron nanoindentor, scan lines from the tip tracking the sample surface were considered. This data can be seen in Figure 2.21. The first image (Figure 2.21a) is taken at a scan rate of 0.1 Hz, and the bottom image (Figure 2.21b) is taken at 3 Hz. There is a drastic difference in the amount of horizontal shift with regards to the scan rate. When the speed of the tool tip increases, the response time of the piezo can not accommodate the surface feature change and the corresponding overshoot is seen in Figure 2.22a. The feedback of lateral motion position is kept at open loop during all experiments, also those in UHV AFM. This is not the case for the normal force feedback, which is controlled by the proportional and integral gain settings in a closed loop system. The piezo is made of Barium Titanate oxide and it is “easier” for the piezo to extend than contract, which is a piezoelectric property of this material. This effect is displayed below in terms of the large shift when the tip is traveling up the slope. This tendency of the tool tip to overshoot and undershoot the actual surface topography is most likely responsible for the ripple propagation. Not only does is continue to “dig deeper” into the troughs and slopes, but this motion also serves to increase the periodicity of the ripples, an effect observed on all samples that produced ripples.

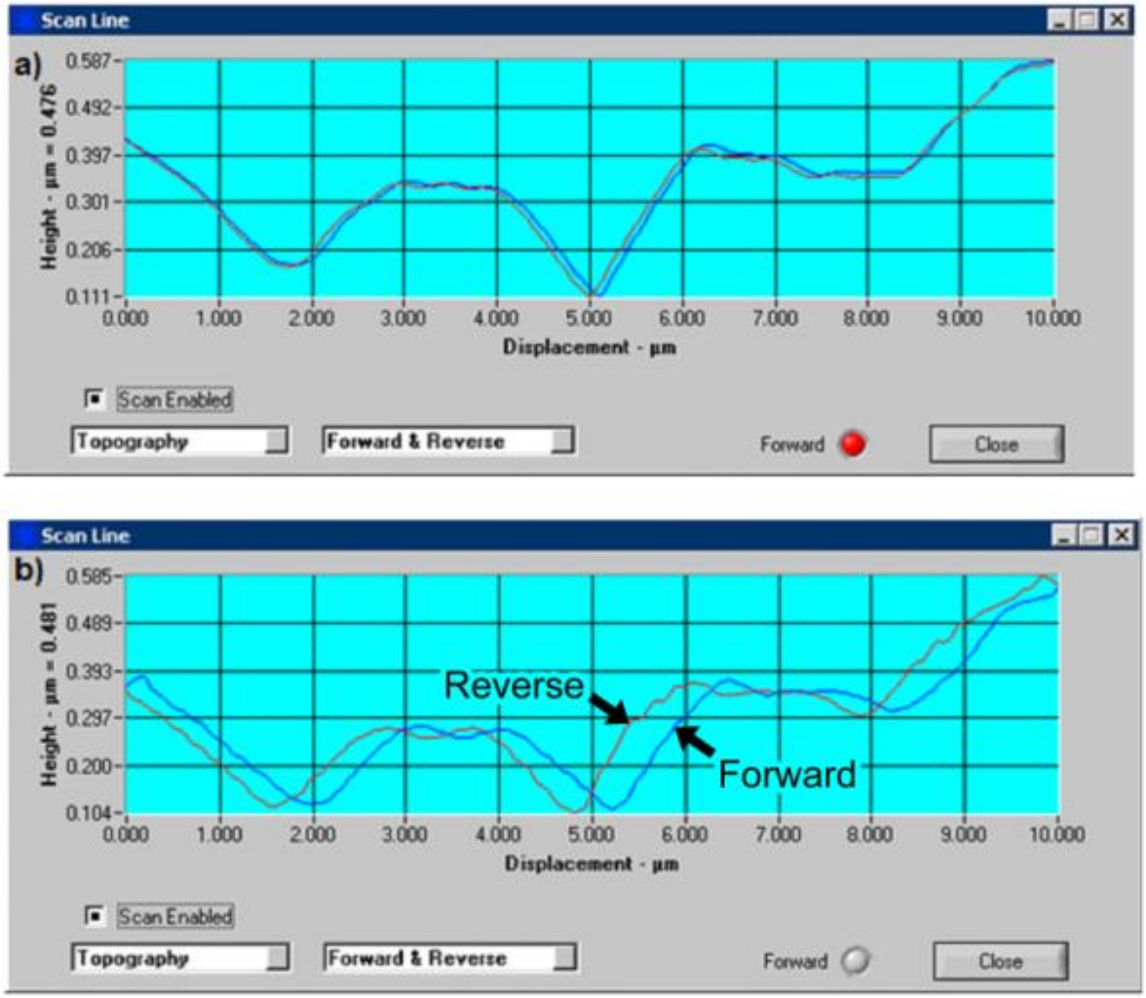

Figure 2.21. Scan lines taken during wear experiments on KBr show the Hysteresis effect heightened by scan rate a) 0.1 Hz b) 3 Hz.

The tip geometry is an inherent source of shift in the forward and backward lines. The forward and reverse scan lines can only ever match up to the diameter of the tip in contact. Figure 2.21a is an example of the horizontal offset of the forward and reverse scan lines due to the tip geometry. Figure 2.21b shows a larger shift, due to the larger role of dynamics in the tip motion.

2.4.3 Inertia Effects

The inertia of the tip also plays a significant role in the path of the tip in its forward and reverse motion. In Figure 2.22a, the blue line represents the path of the tip traveling to the right, and the red line represents the path traveling to the left. The red line clearly shows the geometry of the step height, whereas the blue line shows how the speed, gain, and normal force affect the tip's tracking ability. In relation to the ripple pattern, any topographical step height would be continually propagated as the tip encounters the edge of a step height only when moving up the slope; while moving down the slope the tip does not react quickly enough to cause plastic deformation to both sides of the step height.

Another effect seen in the scan lines taken is "ringing" of the force as the piezo tries to find contact with the sample. Figure 2.22b shows this effect in the red line that records the force in the scan from left to right. When it encounters the "drop off" step height seen in Figure 2.22a, the force oscillates as it tries to maintain constant force on the sample but is out of contact.

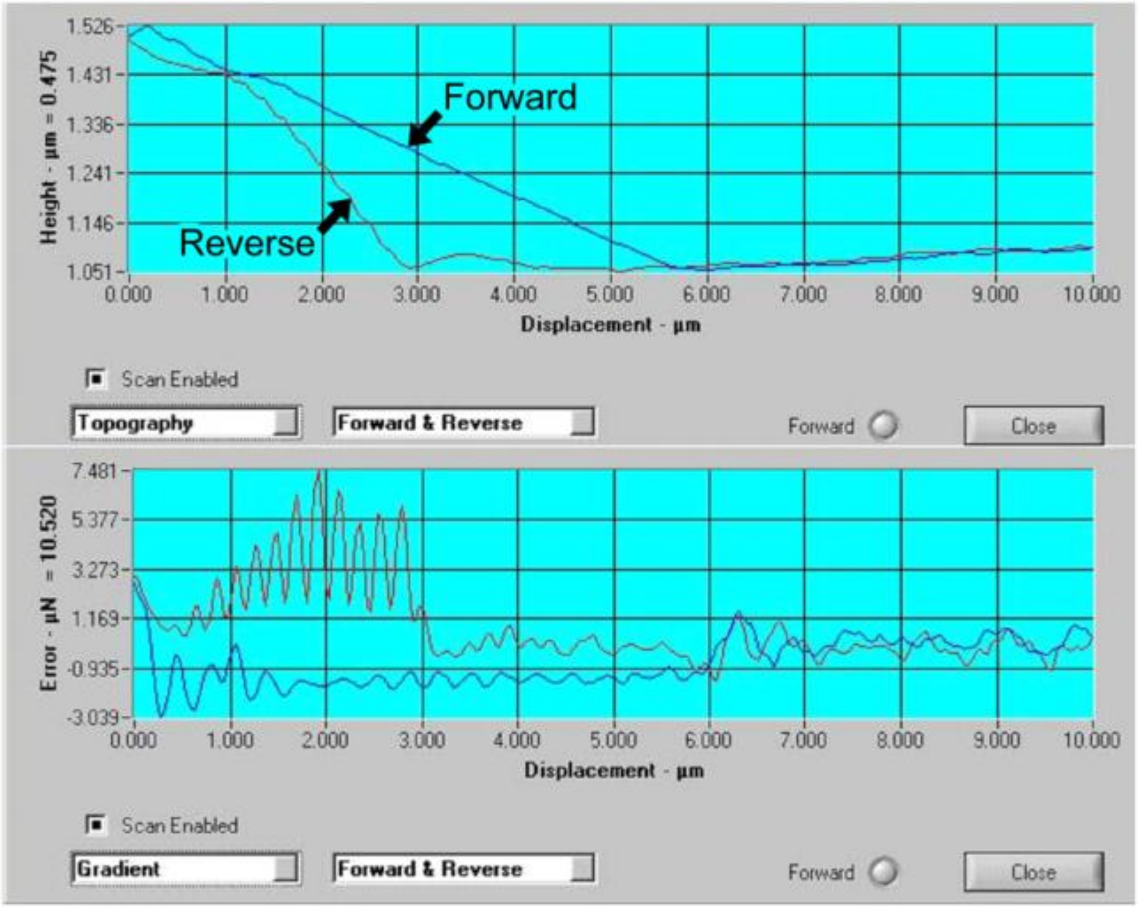

Figure 2.22. Scan lines showing the inertial effects of the tool tip during scanning. a) the overshoot of a step height moving right to left and b) the ringing effect in the normal force.

2.4.4 Forward and Reverse Scan Lines: Horizontal Shift

To gain a better understanding of the tip's motion and reaction to topographical changes, graphs of horizontal shifts were taken to observe any dependencies. Figure 2.23 shows the amount of horizontal shift that occurred on a sample before rippling occurred, and then again after rippling had occurred. The horizontal shift is much greater on the unrippled surfaces, most likely due to inertia effects. It was also of interest to observe if different parts of the scan line experienced different levels of horizontal shift.

Figure 2.24 shows the shift taken at several different points along the sample (high points, low points, relatively un-sloped points) and the dependence of the shift on the scan rate. All areas along the scan show approximately the same level of shift, even as the scan rate increases.

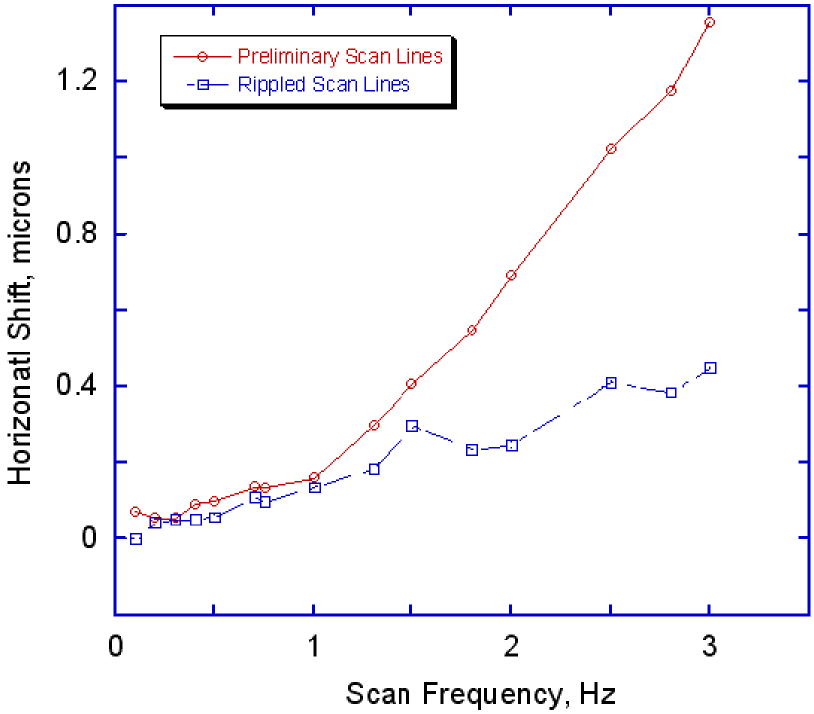

Figure 2.23. Horizontal shift dependence on scan rate and the inertial effect in the preliminary scan line as compared to a rippled scan line.

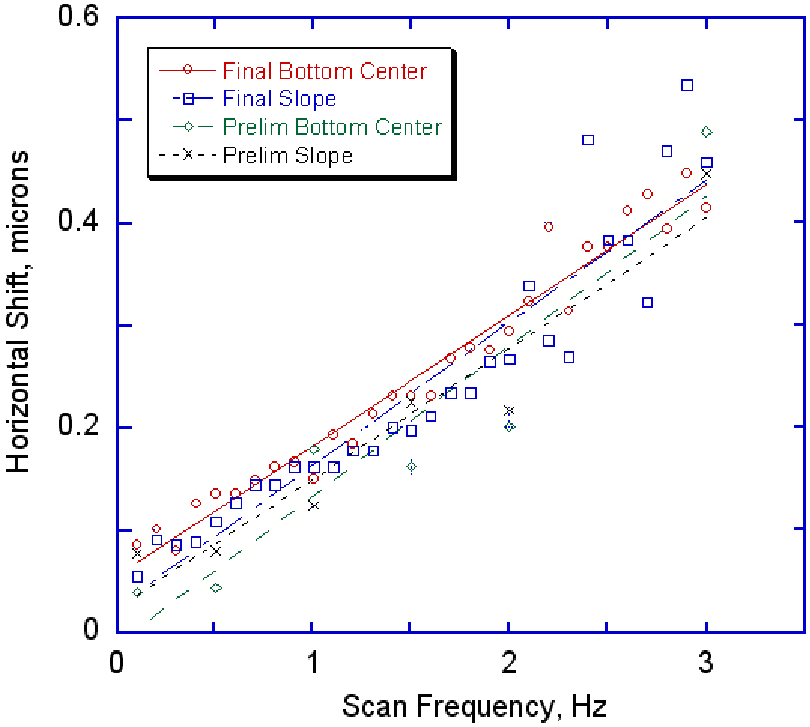

Figure 2.24. The horizontal shift in the scan line and its increase with scan rate taken at different points in the scan line.

2.4.5 KBr Single Crystal Mechanical Properties

An initial theory on the reason for ripple formation was that the tool tip was causing dislocations generation within the crystal. Mechanical properties of KBr were obtained to study the plausibility of the tip providing enough force for causing dislocations. Both quasi static and partial unload indents (Figure 2.25 and 2.26) were performed to gain information about KBr's elastic modulus and hardness (Figure 2.27 and 2.28). The indentation data is interpreted by using the unloading slopes obtained from indentation (Figure 2.25 and 2.26) to achieve values for the hardness of the material (Figure 2.27 and 2.28). The unloading slope is dP/dh, and subsequent hardness values can be obtained from the slope values.

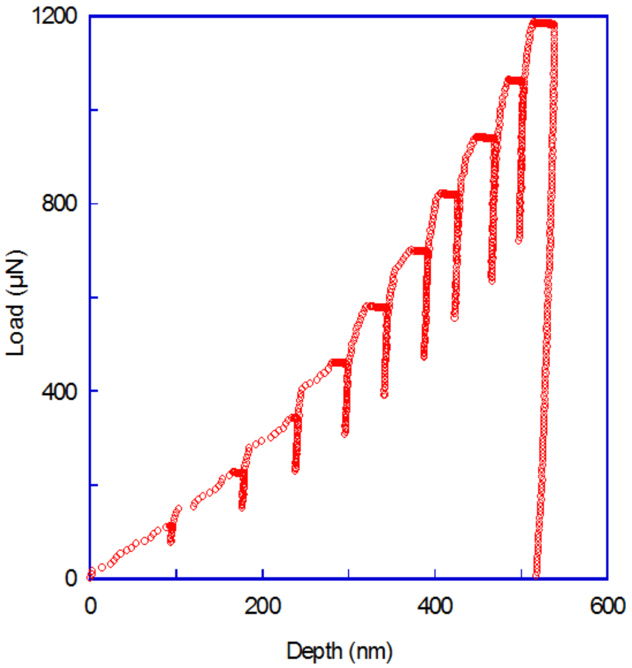

Figure 2.25. Partial unloading data for KBr.

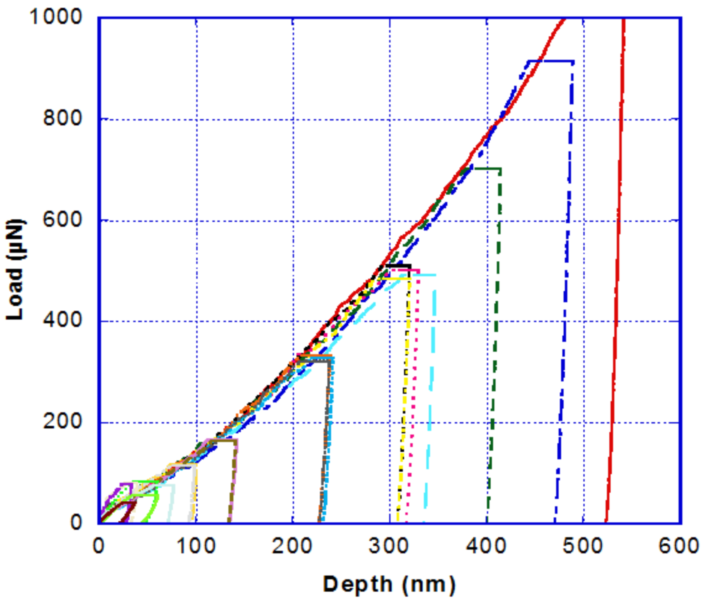

Figure 2.26. Quasi static indentions in KBr.

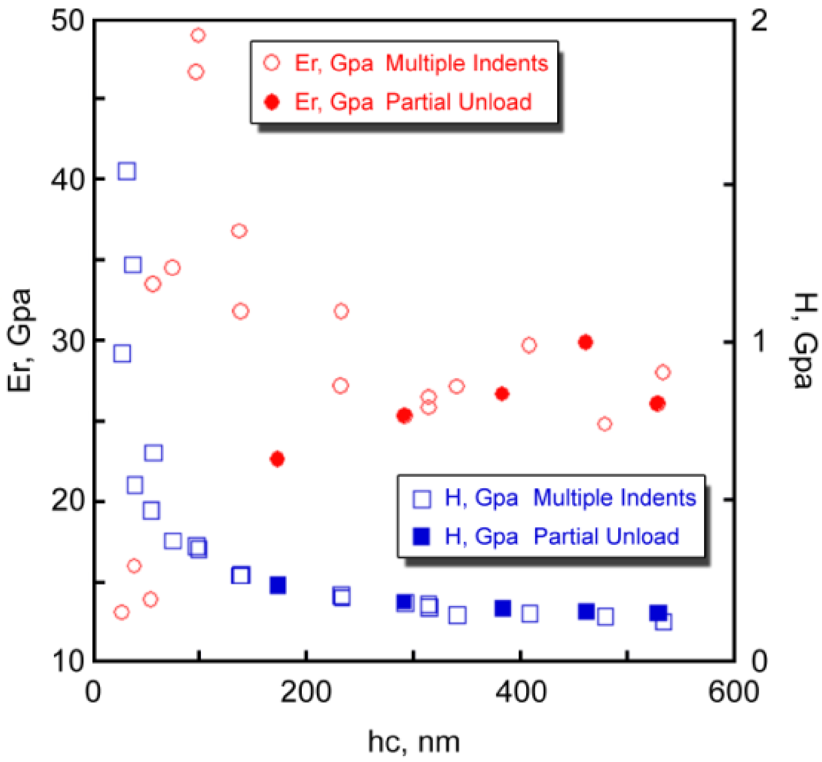

Figure 2.27. KBr mechanical properties corresponding to the partial unloading indents and multiple indents. "hc" is the contact depth.

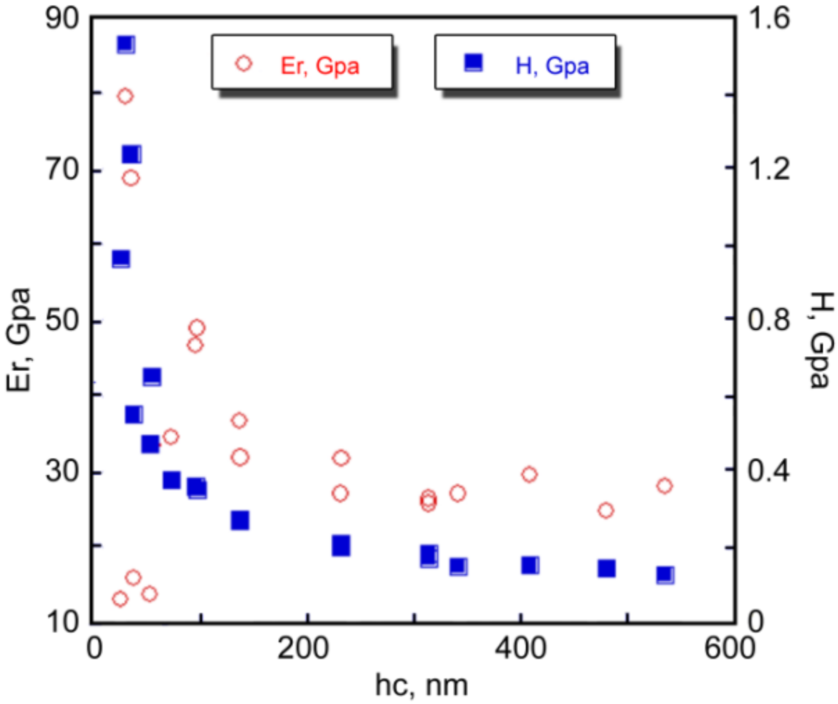

Figure 2.28. KBr mechanical properties corresponding to the quasi static indents.

The higher values for hardness and modulus seen where the indentations were shallow is commonly attributed to "indentation size effect" (ISE). Measurement uncertainty from the small size of the indent causes the higher values obtained for hardness [60]. ISE is also related to the material, not just the ability to measure. The relatively constant value for modulus and hardness after a depth of around 100 nm is expected considering KBr is a bulk single crystal material. Other materials, particularly thin films, often show substrate effects that influence the hardness and modulus results so the data does not look like a horizontal line after a certain depth.

Zooming in on the lower left side portion of Figure 2.28 shows the load controlled indent data for KBr (Figure 2.29). The horizontal portions of the graph show where a dislocation was emitted and the tip dropped further down into the sample. If the tip is able to produce forces like this during scanning, dislocations could be influencing pattern formation.

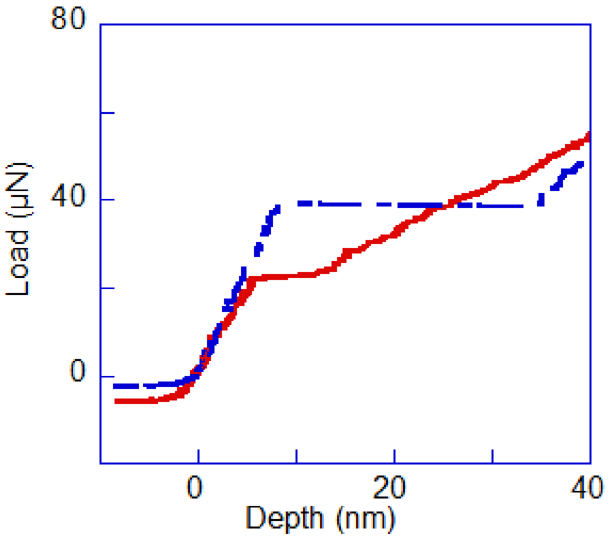

Figure 2.29. Load controlled indents showing load excursions associated with dislocations being emitted.

After gathering data on the mechanical properties of KBr, it became necessary to have an accurate tip area to make appropriate calculations. Figure 2.30 is an AFM image of a tip, which when cross sectioned, produces Figure 2.31, and the area of the tip can be found.

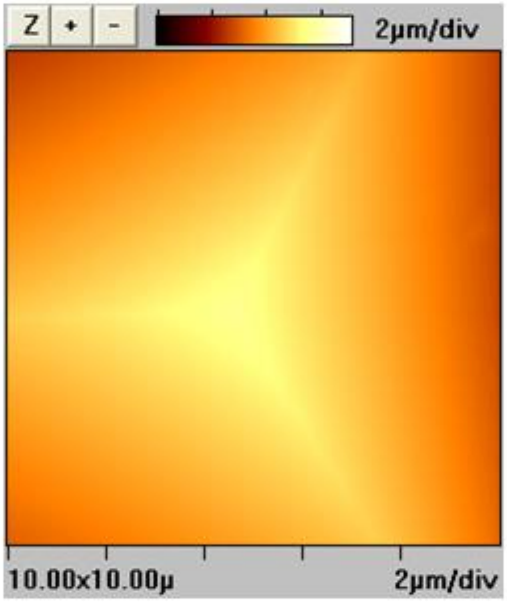

Figure 2.30. An AFM image of a tip.

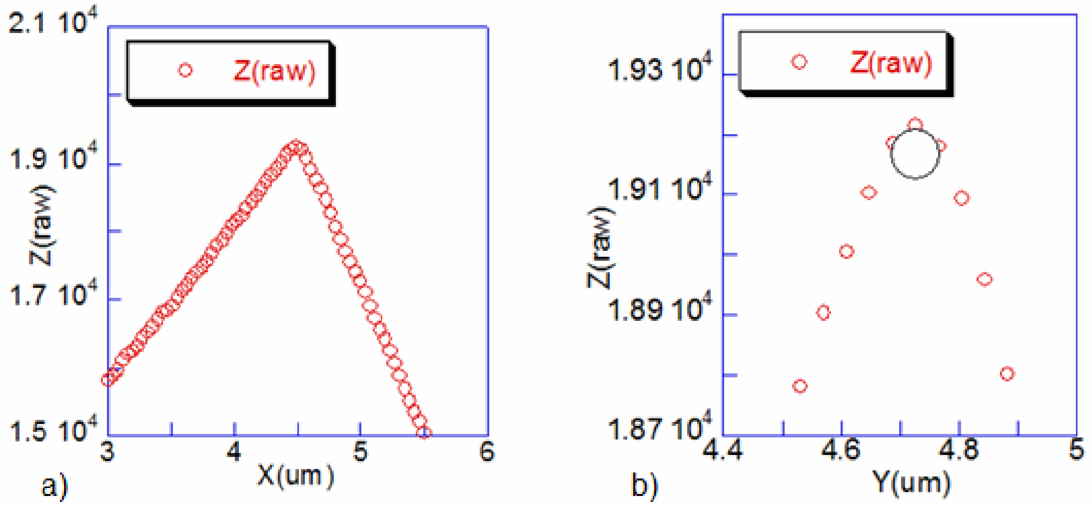

Figure 2.31. a) Cross section geometry of a tip, b) zoomed in to find tip diameter.

Based on the KBr load-displacement data, it is possible to create dislocations at 2 μN normal scanning force, especially since KBr is a low hardness material. Load-displacement discontinuities with regard to normal force were seen during nanoindentation experiments at 5 nm of depth with a 20 μN normal load (Figure 2.29). With the addition of a shear stress component during scanning, smaller normal load of 2 μN could be enough to induce dislocations, as only 2.5 GPa shear stress is required.

2.4.6 Chatter

Another possibility of the formation of ripples is that the tool itself causes either forced or self-excited vibration (equivalent of chatter observed at the macroscopic scale) [64]. All ripple experiments over an area were performed with a low gain setting, a parameter that affects how well the Proportional, Integral, Derivative (PID) controller forces the tip to "track" the surface topography. The tip deepens low surface points with each consequent contact. The transducer resonance frequency is around 130 Hz, orders of magnitude higher than the image scan rate of 1-3 Hz. The higher the scan rate, the more likely the tool will strike the surface at the same rate of the natural frequency of some other system parts, whether it be the piezo, tip holder, etc., contributing to the formation of ripples. Figure 2.29 is a macroscale example of how speed and force are influential in producing chatter. There are relative "sweet spots" where no chatter is seen, and this parallels experiments where changing scanning speed, normal load, or gain settings did not produce rippling. During the wear experiments the tip maintains contact with the surface until the desired number of passes programmed has been reached. Similarly, in milling and turning macroscale processes, where the cutting tool is not removed from the surface, chatter can be seen in the regeneration of waviness continued by the periodic force induced by the already wavy surface. Mode coupling is another source of self-excited vibration that produces chatter when these vibrations are in planes positioned perpendicular to the cut, or wear path in these experiments. However, consequences of the generally small size of the test area dictate that bulk material physics do not dominate; instead, surface forces play the main role in determining characteristics of the materials reaction [4]. From the ripple data of Figure 2.2, the tip speed is 24 μm/s, and a ripple occurs every 0.63 μm. This is a ripple frequency of 39 Hz, much lower than the transducer resonance frequency of 130 Hz, so chatter is not a well supported possibility for ripple formation.

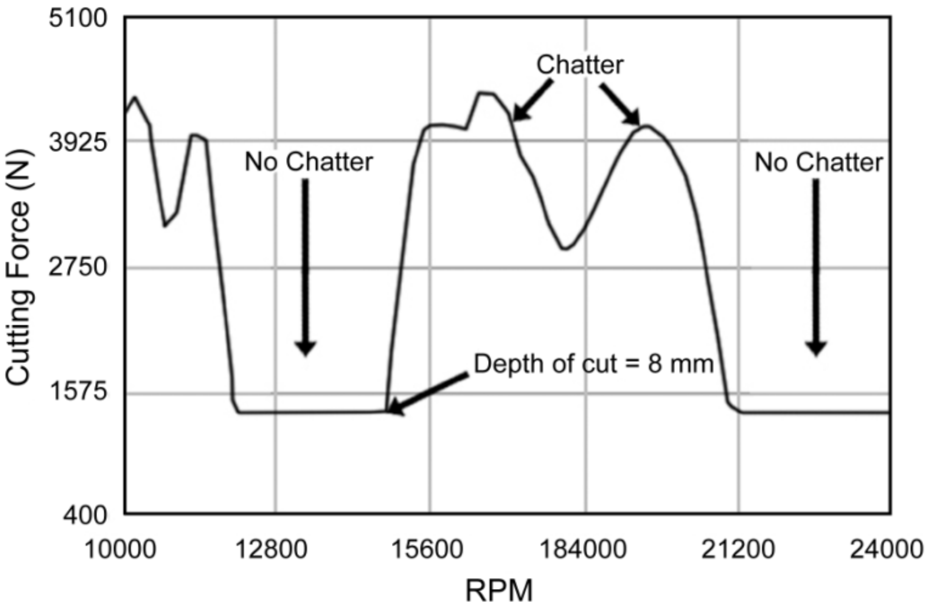

Figure 2.32. An example of how chatter varies with speed and normal load applied.

CHAPTER 3

WEAR TESTING IN VARYING ENVIRONMENTS

3.1 Introduction to Environmental Wear Dependence

A focus of this chapter is wear testing in a liquid environment. It has been shown in practical applications that humidity can have an impact on wear of metals [66]. Conflicting situations have been observed, where some experiments show an increase in wear rate with increasing humidity, while others experience a decrease in wear rate with an increase in humidity [7, 8, 67].

Experiments performed on 3 μm sputtered gold samples showed 3 times higher wear rate in water than at ambient humidity (approximately 55%). These experiments were performed in the Hysitron Nanoindenter and results are in section 3.3. It was of interest to repeat this experiment in the Atomic Force Microscope to observe if the same results would be achieved. This would elucidate if the results were a feature of the scanning properties of the Nanoindenter, or a property of the gold sample.

3.2 Experimental Details of Environmental Testing

For wear testing in the AFM, contact mode tips were used. These are dual cantilevered to supply the extra strength for the higher loads of contact scanning. Tapping mode tips mainly used for sensitive cellular material have a single cantilever geometry (Figure 3.1a). For contact mode scanning in water, some adjustments need to be made for testing with a fluid cell using AFM. Most fluid cells are designed for biological samples, using a large triangular compliant tip. This provides a large area for the laser to reflect off and helps with aligning the detector. In the wear experiments it is necessary to use a stiffer cantilever that has a smaller surface area. To be able to get a large enough laser signal in the detector, the tip must be positioned slightly tilted to direct the laser beam into the detector. The glass over the fluid cell also refracts the laser signal, producing an approximate 30% drop in total signal with the glass in place. Another issue in working with AFM is that the laser signal can be scattered by the sample surface and further deteriorate the signal strength [29].

Figure 3.1. Schematic of a) tapping mode tip and b) contact mode tip (dual cantilever).

Sputtered gold films, 3 μm thick were cleaned with acetone and methanol before conducting AFM and Hysitron wear tests. The Hysitron experiments were preformed with a conical diamond tip (1 μm tip radius). The AFM tip was a silicon nitride cantilever with a radius of 100 nm. The Hysitron experiments were performed with a normal load of 10 μN, while the AFM experiments were performed at 2 μN. Test parameters were kept the same when testing in ambient atmosphere (55% humidity) or in a distilled water environment. Test area in the Hysitron was 10x10 μm^2 and 1x1 μm^2 in the AFM.

3.3 Wear in Water Compared to Ambient Conditions

Figure 3.2 shows results of wear testing in the ambient environment in the AFM. From the topography and cross section of the gold, it is apparent that there is minimal wear, on the order of 5 nm. There is surface modification or smoothing of asperities that appears in the ambient environment experiments. Results obtained in the Hysitron Triboindenter also displayed minimal wear on the order of approximately 15 nm (Figure 3.4.

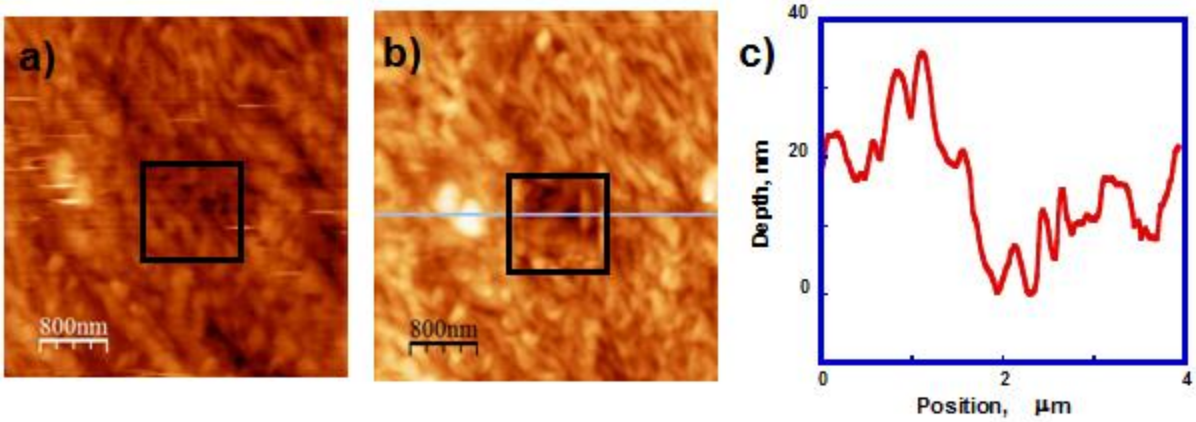

Figure 3.2. Sputtered gold film tested in ambient environment in AFM at 2 μN normal load, 10 Hz, 1x1 μm^2 scan area. a) Initial surface with a square outlining the wear test area; b) Surface after 30 scans with the same identifying square; c) Cross-section of b showing depth reached in the scan area.

Figure 3.3 shows the results of the wear tests performed in the presence of water in the AFM. Compared to the previous ambient experiment, the test in water was performed for the same number of scans and produced a depth of 20 times greater than in the ambient experiments. Depth values were taken at the center of each wear scan to accurately obtain the depth over different images. Experiments performed in the Hysitron Tribolindenter were performed for half the number of scans as the ambient experiment, and similarly to AFM results, produced 10 times higher wear rate. The wear tests performed in the Hysitron can be seen in Figures 3.4 and 3.5.

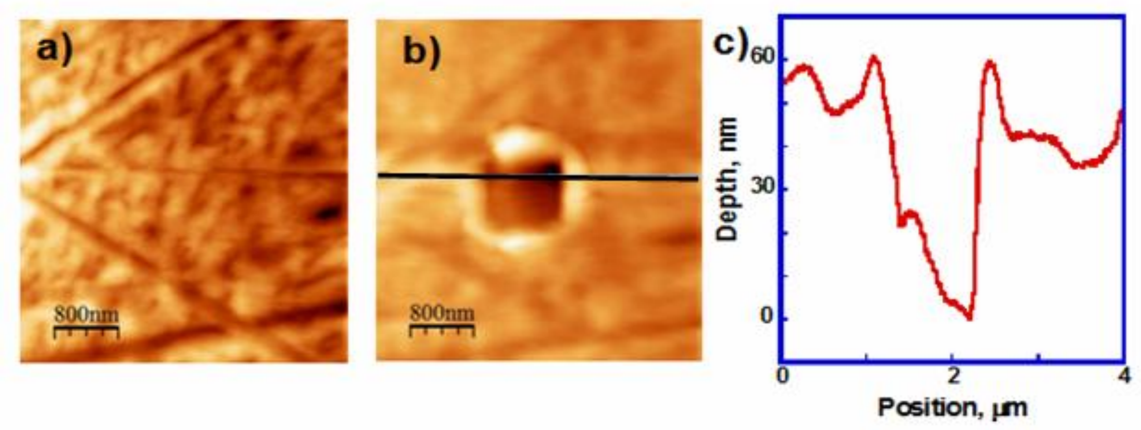

Figure 3.3. Sputtered gold film on silicon scanned over a 1x1 µm^2 area in AFM for 30 scans at 10 Hz, 2 µN normal load in the presence of water. a) Initial surface; b) surface after 30 scans; c) cross-section showing depth reached in the scan area.

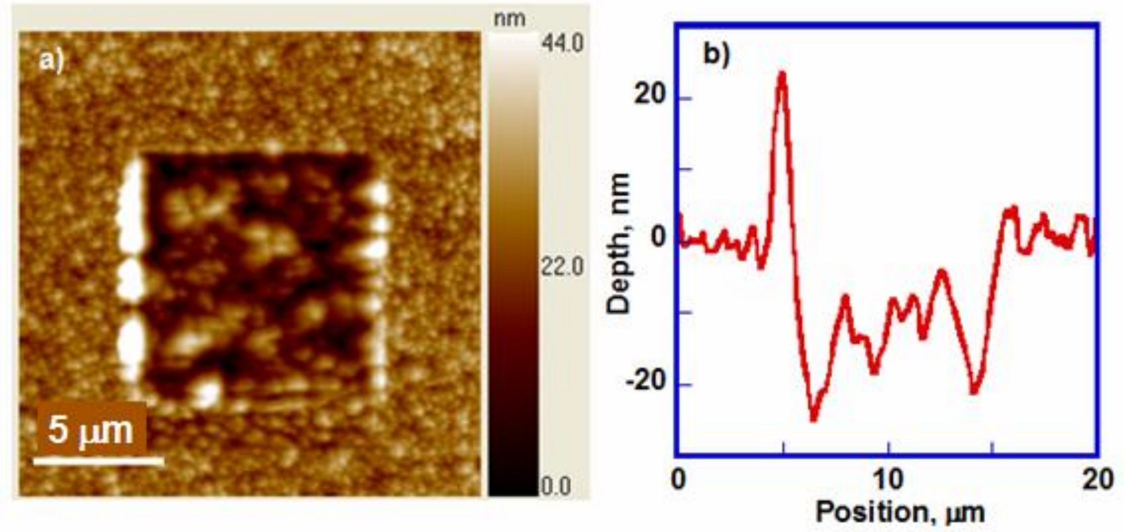

Figure 3.4. a) Wear area and b) Wear track topography of a gold film after 200 wear cycles at 10 µN normal load with a blunt conical tip in air. Courtesy of Xialou Pang, University of South Florida.

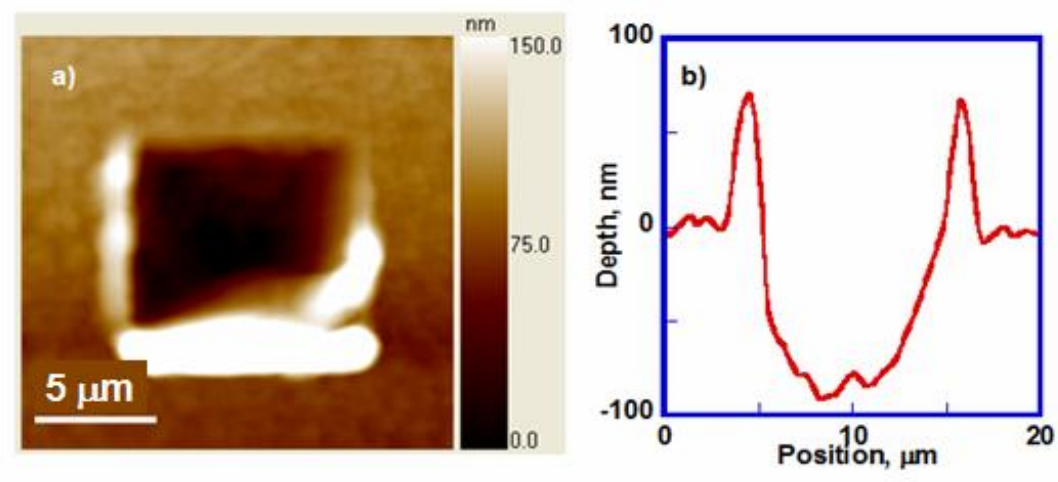

Figure 3.5. a) Wear area and b) Wear track of a gold sputtered film after 100 wear cycles at 10 µN normal load with a blunt conical tip in water. Courtesy of Xialou Pang, University of South Florida.

Figure 3.6 shows the wear depth versus the number of scans for both wet and ambient conditions from the AFM experiments. It would be ideal to have more data and continue the test for a larger number of scans, but experimenting in water without a fluid cell requires the test to be performed before the water on the sample evaporates; only allowing a small number of scans. The addition of water to try to avoid this short scanning time proved only to make the tip lose contact with the sample due to the capillary forces of the added water. This loss of contact provides an offset and the test can not be continued in the exact same area.

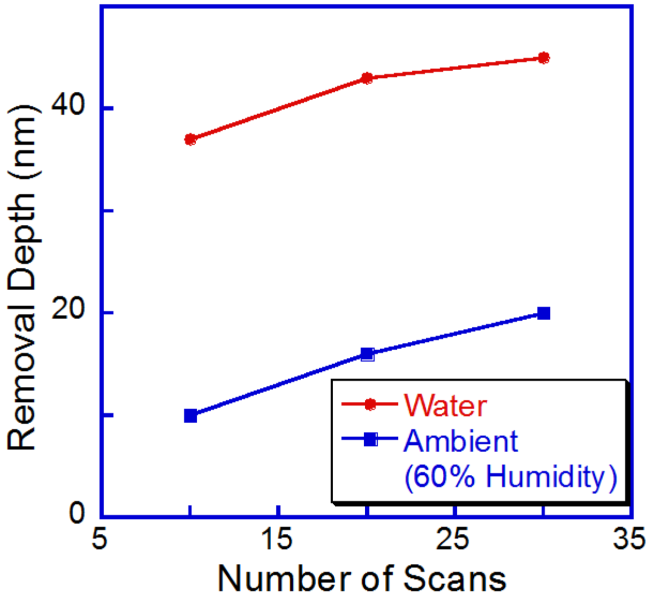

Figure 3.6. Data obtained from experiments performed on the AFM in water and ambient conditions.

This drastic increase in material removal observed in the experiments performed in the presence of water could possibly be due to moisture-assisted grains fracture and pull-off, with more material going into solution and increasing friction. An additional test preformed was scanning a single line repeatedly in the AFM to obtain an idea of the wear rate corresponding to the depth. An example of this can be seen in Figure 3.7a. The depth of scan lines (Figure 3.8) possibly plateaus at a certain depth even when the number of line scans continually increases (more data would be needed to conclusively describe a plateau). With constant normal load the tip contact area is increasing during abrasive wear, until the contact pressure is reduced below the level of gold hardness, at which point the wear process transitions from abrasive to frictional wear. Figure 3.7a displays 2 single scan line wear tracks, the one on the left tested for less than 500 scans and the right scan tested for less than 250 scans. Other scan parameters were kept equivalent at 200 nm scan length, 20 Hz speed, 0.1 integral gain value, and 2000 nN.

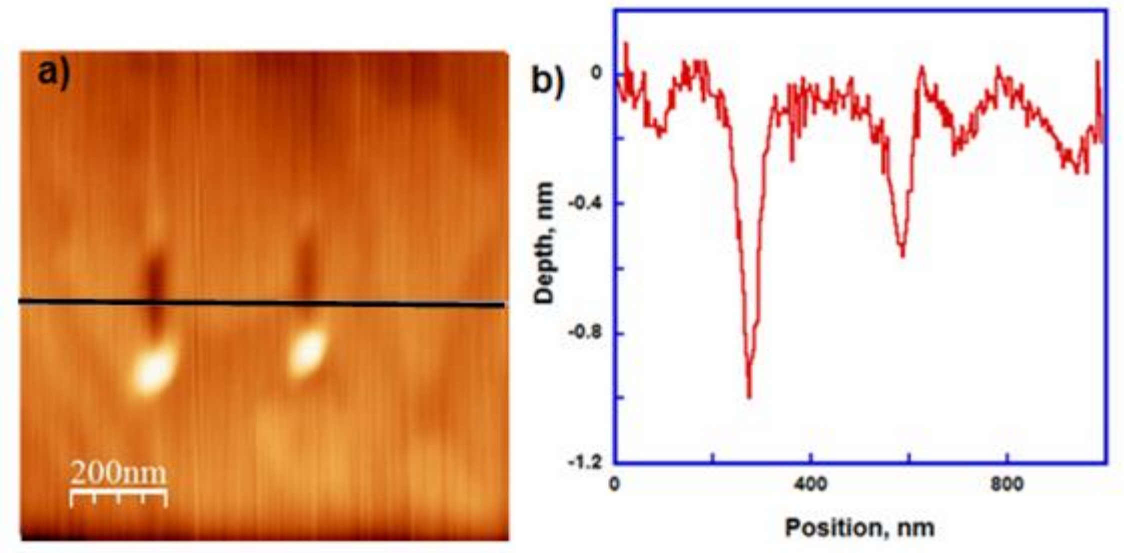

Figure 3.7. a) An example of the single scan line wear performed on the single crystal gold and b) the profile view showing the depth of scan lines.

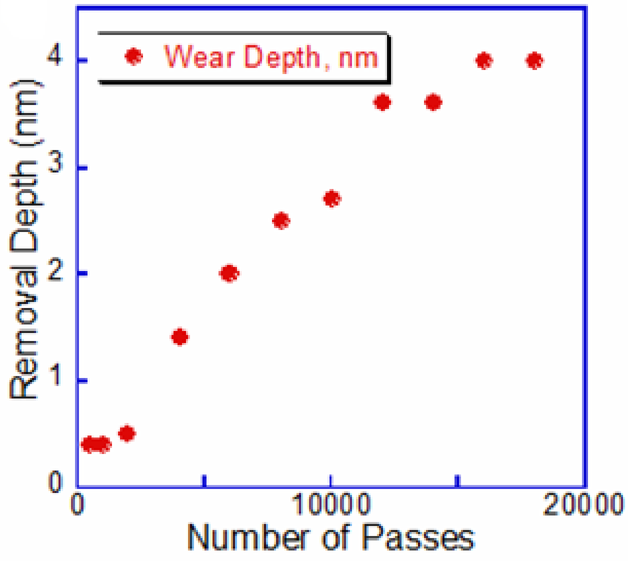

Figure 3.8. Single scan line wear data portraying the possible "plateau effect" after initial rapid wear.

As previously mentioned, most wear tests performed in the ambient environment only smoothed out asperities on the surface of the gold, as can be seen in the progressively scanned images in Figure 3.9.

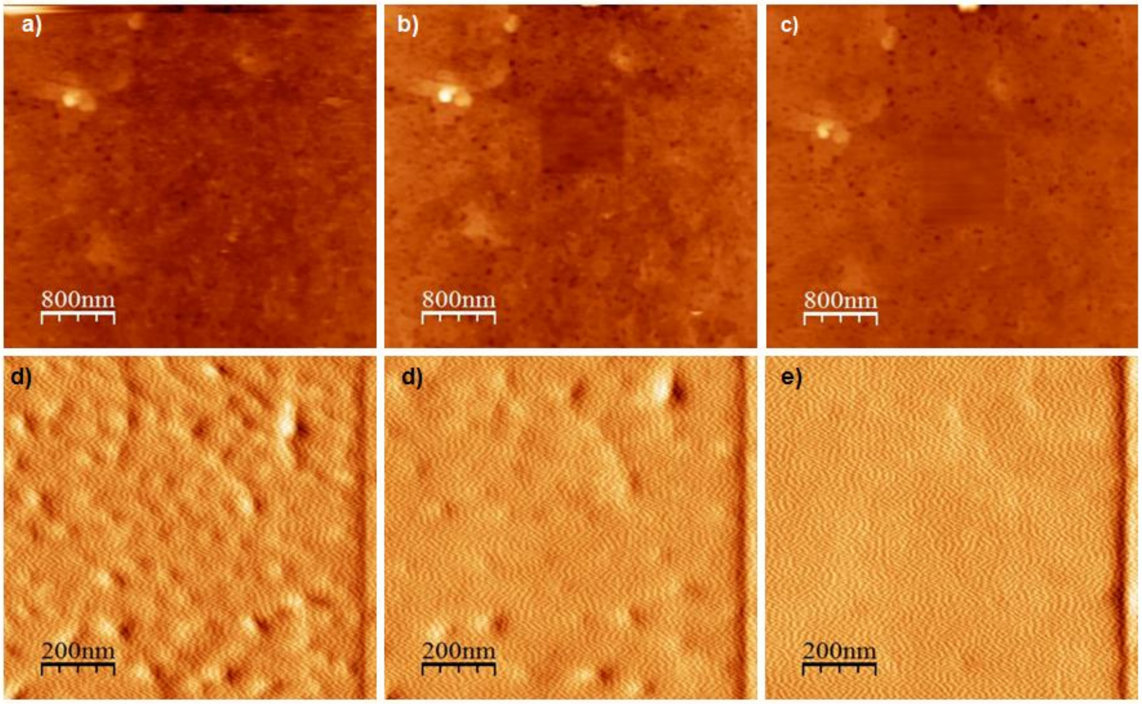

Figure 3.9. 200 nm thick evaporated gold film on mica. a) Initial surface topography. b) After 10 scans at 10 Hz, 2000 nN Normal load, 1x1 μm^2 scan area; c) After 10 additional scans; d) Initial deflection image of the scanned area (1x1 μm^2) and e) after 10 scans, and f) after 10 additional scans.

3.4 AFM Wear of KBr

The ability to reproduce the ripple pattern seen in the UHV AFM in the ambient Hysitron nanoindenter inspired experiments to reproduce ripples in the ambient AFM. However, these wear tests produced typical wear areas, as seen in Figure 3.10 and 3.11.

Rippling was usually initiated in the Hysitron at cleavage steps on the sample, and wear testing in the AFM only smoothed the cleavage steps, as seen in the progressive images of Figure 3.11.

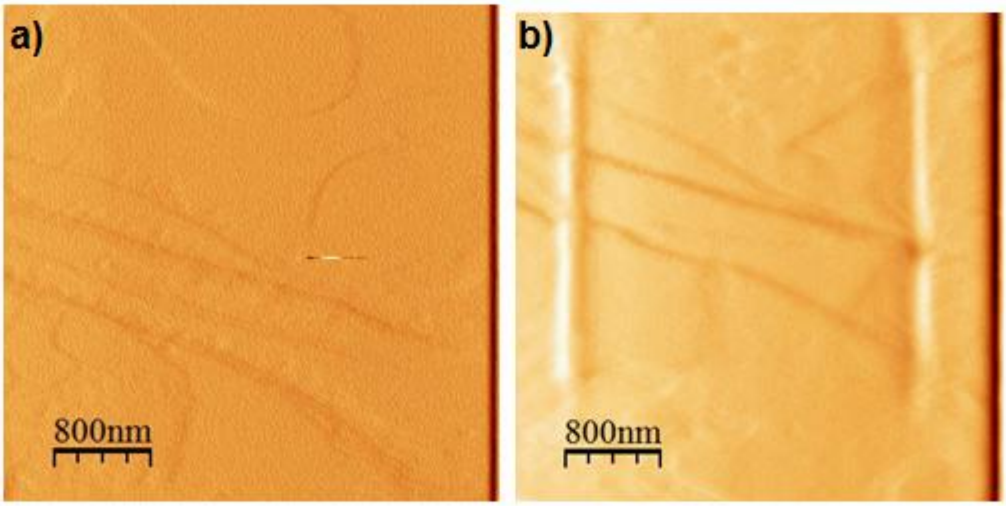

Figure 3.10. KBr scanned at 1000 nN, 10 Hz, over a 3x3 μm^2 area and b) wear area after 25 scans.

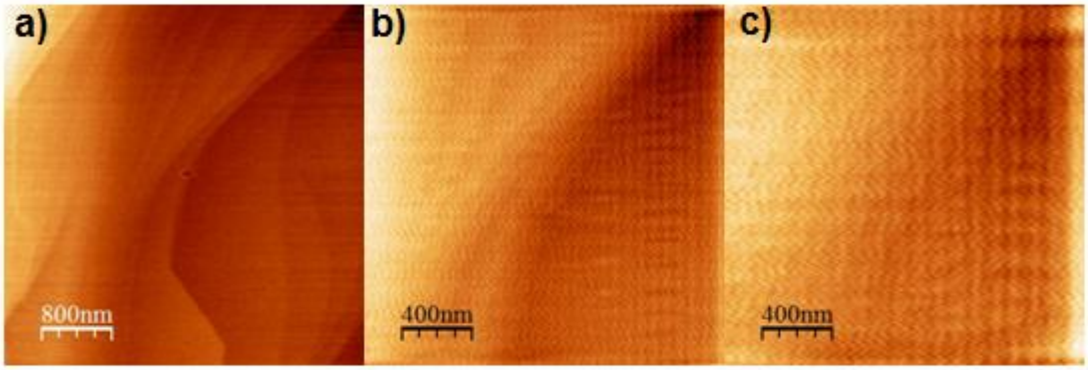

Figure 3.11. Wear test of KBr tested at 500 nN at 10 Hz, over a 2x2 μm^2 area. a) The initial image b) a zoomed in image during scanning after 20 scans and c) the same area after 150 total scans.

A wear test of KBr and corresponding profile of the wear area can been seen in Figures 3.12 and 3.13. The profile in Figure 3.13 shows the large pile up structures that were formed. The pile up structures in this experiment are very large, due to the material being plastically pushed to the edges of the wear scan. In experiments that produced the ripple pattern, the pile up structures were not as large, because the material was spread out over the wear area forming the ripples.

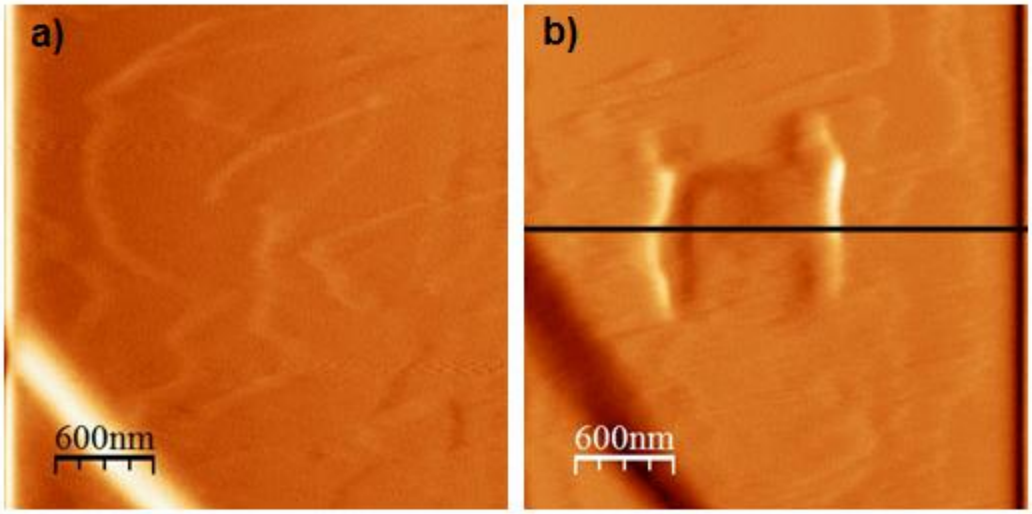

Figure 3.12. a) Initial KBr surface before being scanned at 15 Hz, 1000 nN, over a 1x1 μm^2 area for 10 scans. b) Final image showing wear area.

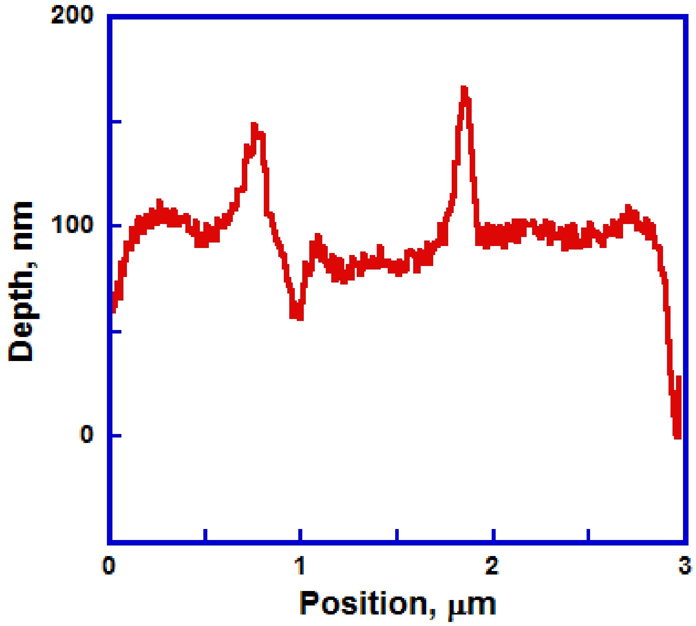

Figure 3.13. Profile of KBr wear test performed in the AFM. Substantial pile up features were produced, but no ripple pattern formed.

3.5 Surface Contaminants

On particularly humid days (> 60%) the surface of NaCl appeared to be contaminated, possibly with water droplets or debris from the air (Figure 3.14).

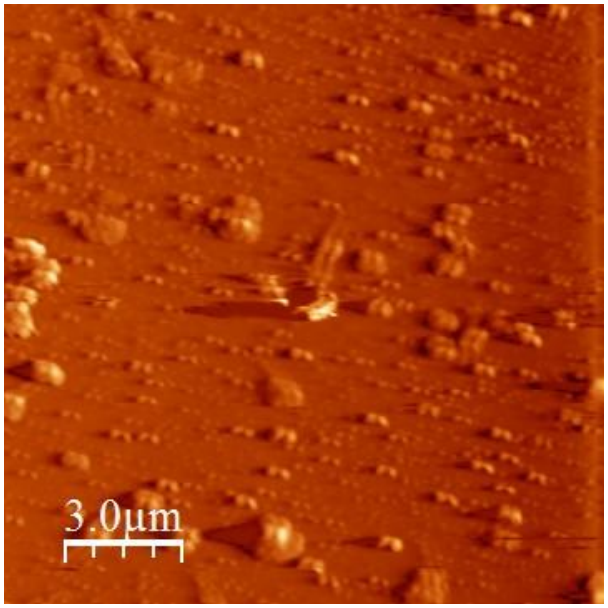

Figure 3.14. A 15x15 μm^2 image of NaCl showing the surface contaminants.

The damage in the center of Figure 3.13 is due to the tip initially making contact with the sample in that area.

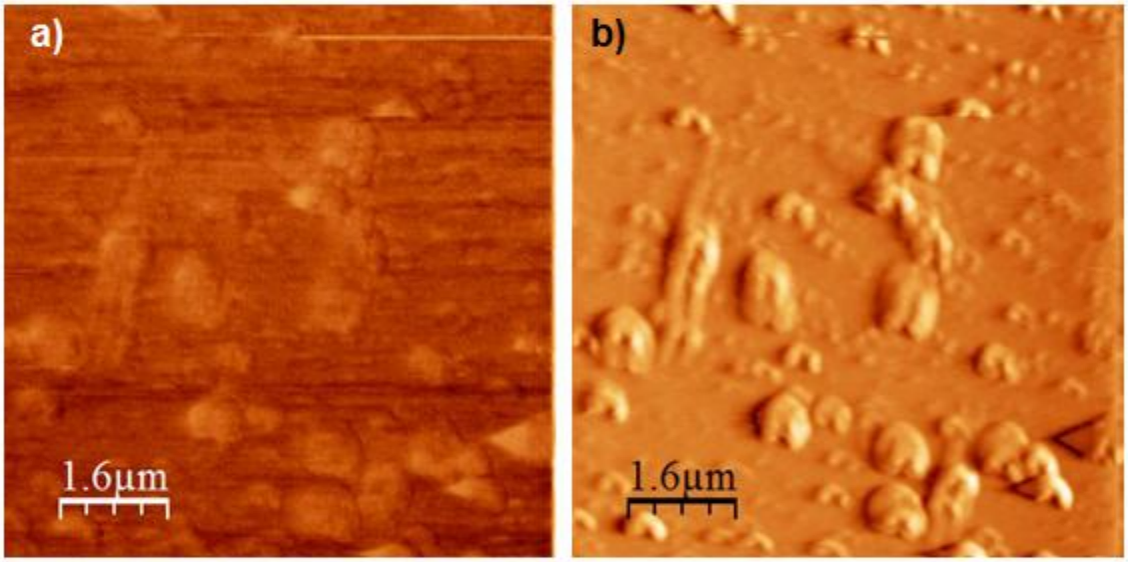

Figure 3.15. Zoomed in 8x8 μm^2 image of the contaminants, a) Topography image b) Error signal image shown for clarity.

A wear test was performed to determine whether or not the contaminants could simply be swept away, or if it was attached to the crystal. As Figure 3.16 shows, the contaminants were not simply swept away, but appeared slightly smoothed out after 32 scans at 1500 nN normal load.

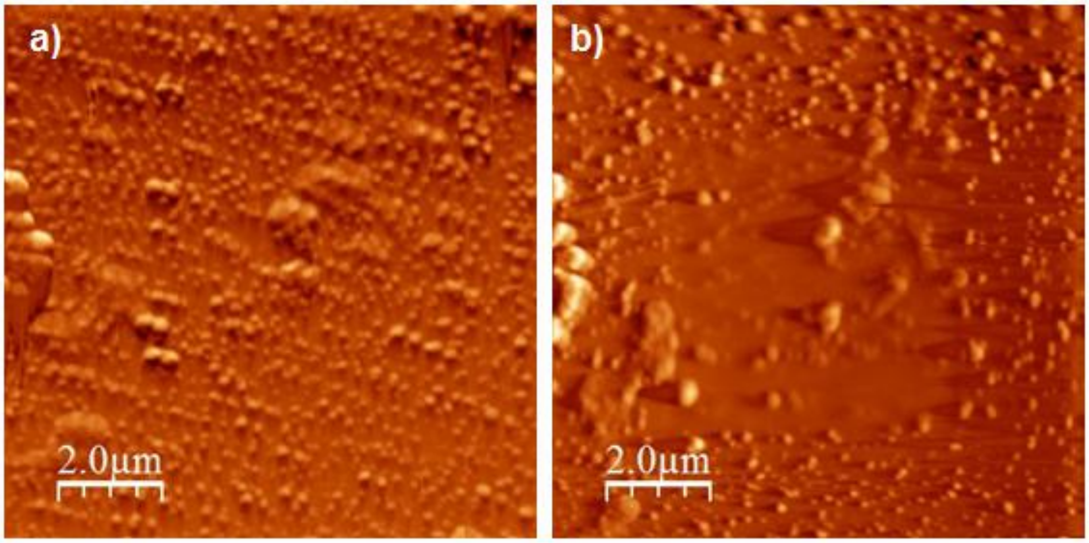

Figure 3.16. Scanning a 5x5 μm^2 area at 7 Hz speed and 1500 nN normal load for 32 scans. a) Initial topography b) final image.

To ensure that this was not a property of the salt crystal, a 3 µm thick sputtered gold sample was scanned and similar results were obtained (Figure 3.17).

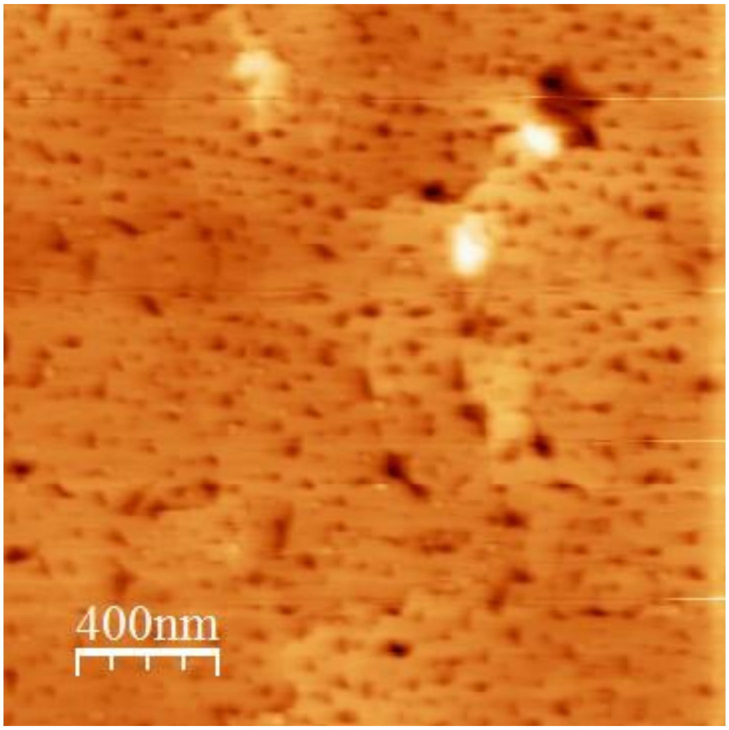

Figure 3.17. 3 μm sputtered gold displaying contaminants. These are microstructure features.

After the NaCl and gold surface contaminants were observed (Figure 3.15-3.17), the sample was switched to a freshly cleaved KBr sample that did not display any of the surface texture. However, upon testing, it appeared that all 3 tips were in contact with the sample, or significant amounts of the surface contaminants had adhered to the tips making them large enough to come in contact with the sample. Figure 3.18 is an example of the tip set up, and Figure 3.19 displays an example of the three wear tracks.

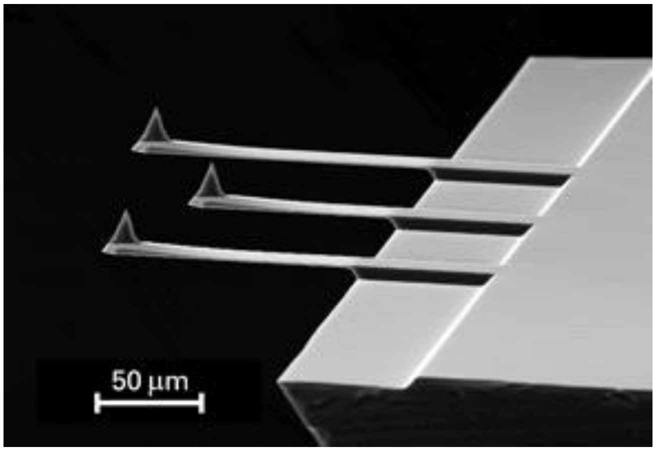

Figure 3.18. Examples of the 3 tip set up.

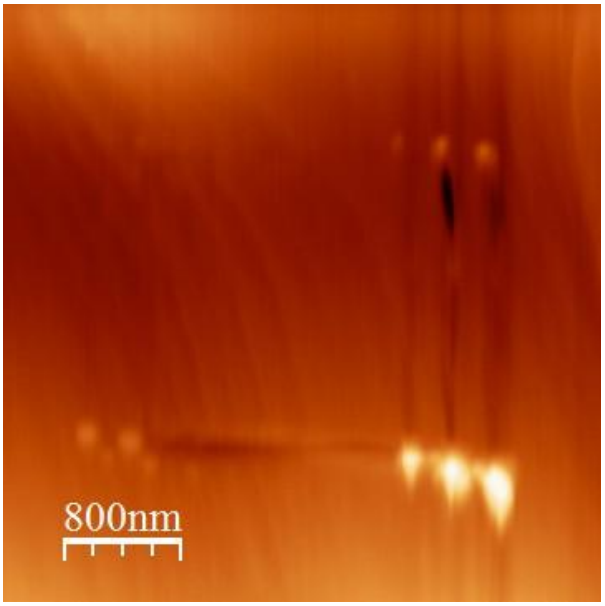

Figure 3.19. KBr wear track showing 3 wear tracks on the right side.

The sample was then scanned at an angle to observe if the situation was directionally dependent. Figure 3.20 shows that even scanning at 45 degrees the other tips are still marring the surface.

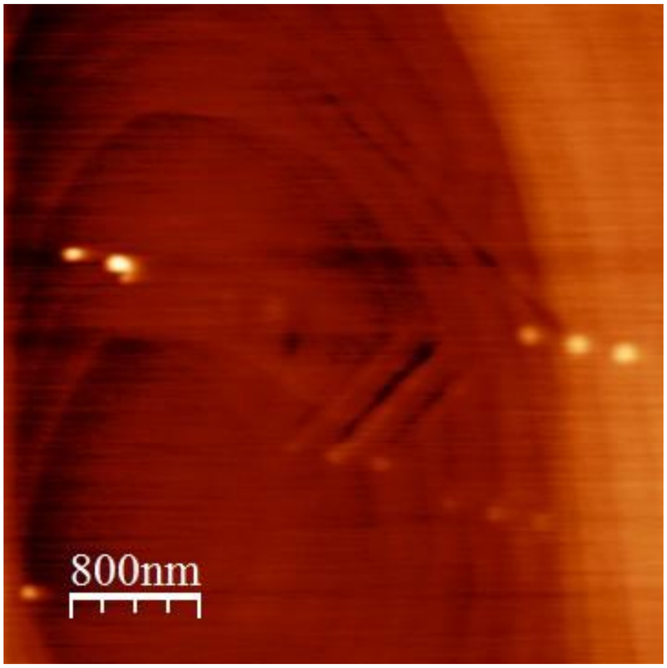

Figure 3.20. KBr surface proving that the “3 tip” image was not vertically dependent, as the lines appear when scanning is oriented at 45 degrees.

Eventually, the square wear area became distorted (Figure 3.21).

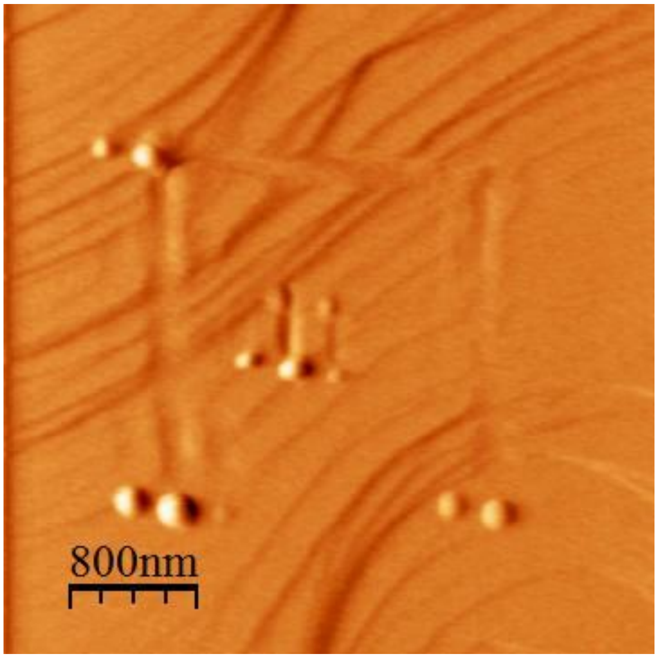

Figure 3.21. An example of the distortion seen during the multiple tip engagement behavior. The wear track should show a perfectly square outline.

3.6 Single Crystal Gold Wear

In scanning single crystal gold, the wear test served to remove layers, as seen in Figure 3.22.

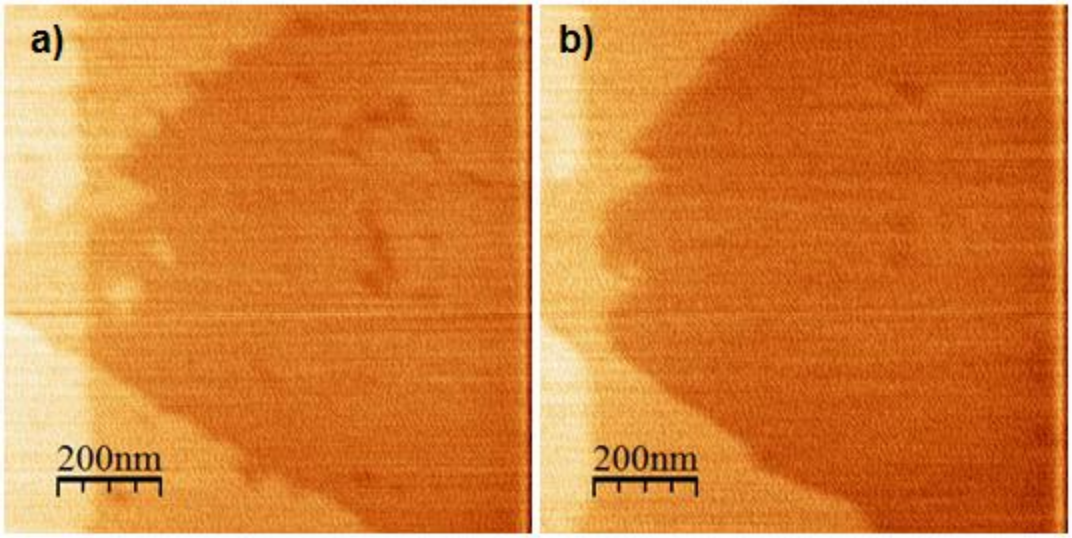

Figure 3.22. Single crystal gold wear test at 5 Hz speed, 200 nN normal load at a gain of 0.5 over a 1x1 μm^2 area. A) Original surface and B) Surface after 10 scans.

Performing the wear test on single crystal gold produced higher wear, as can be seen in the progressive images taken in Figures 3.24 and 3.25. This test was performed at 750 nN at 10 Hz scan speed. Approximately half way through the 350 scans, a ripple pattern appeared in the test area (Figure 3.23). These ripples did not propagate much, as Figure 3.21a and 3.21b were taken 50 scans apart.

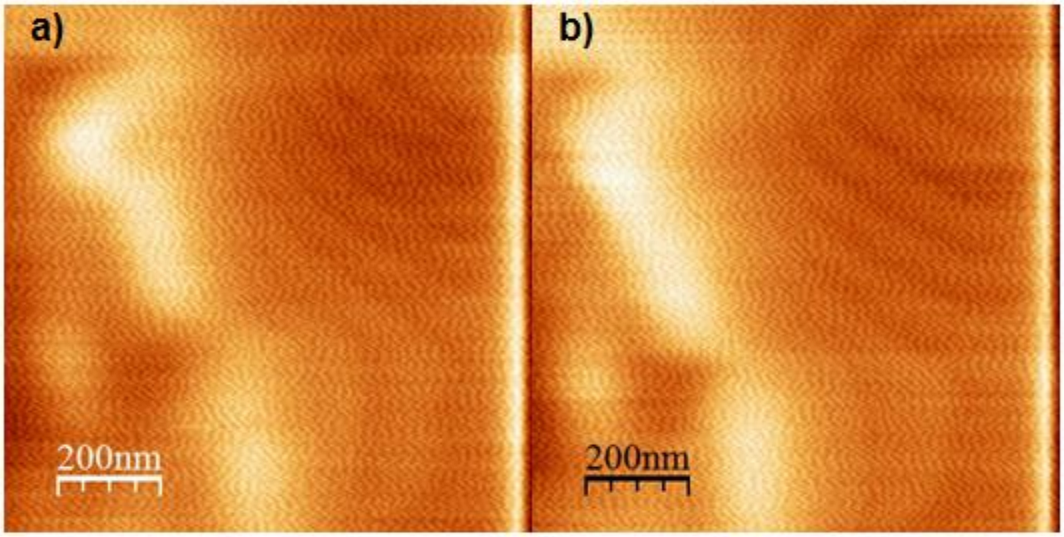

Figure 3.23. Appearance of what could be small ripples propagating from the upper right corner of the scan area. a) after 230 scans b) after 280 scans.

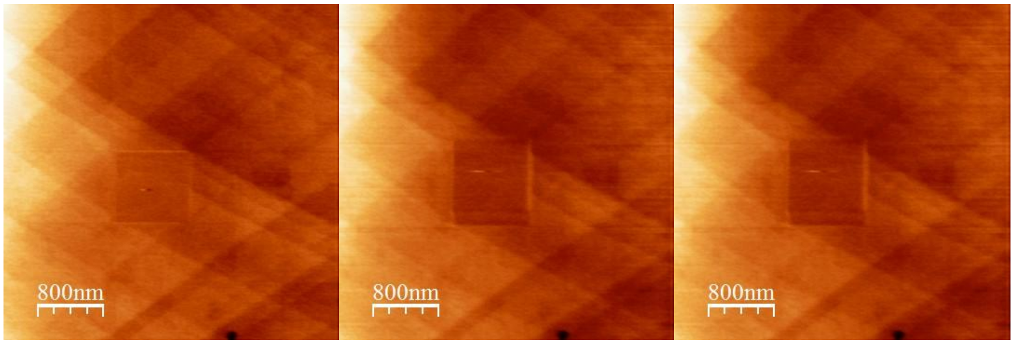

Figure 3.24. Progressive images of single crystal gold throughout a wear test.

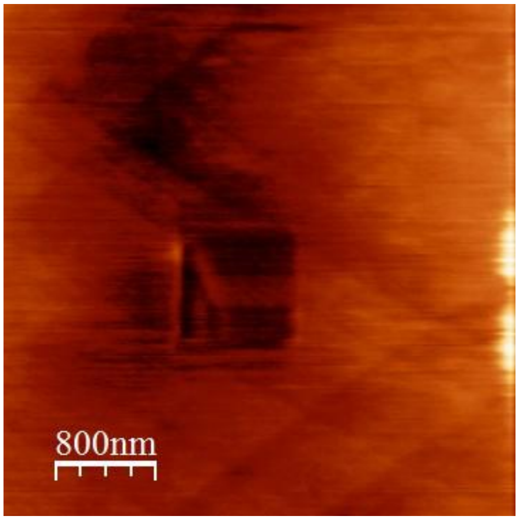

Figure 3.25. The final image of the single crystal gold wear test.

The single crystal gold did not hold up well in tests at higher normal loads for many scans. The following figures display the results of a 1000 nN normal load scan for 10 scans.

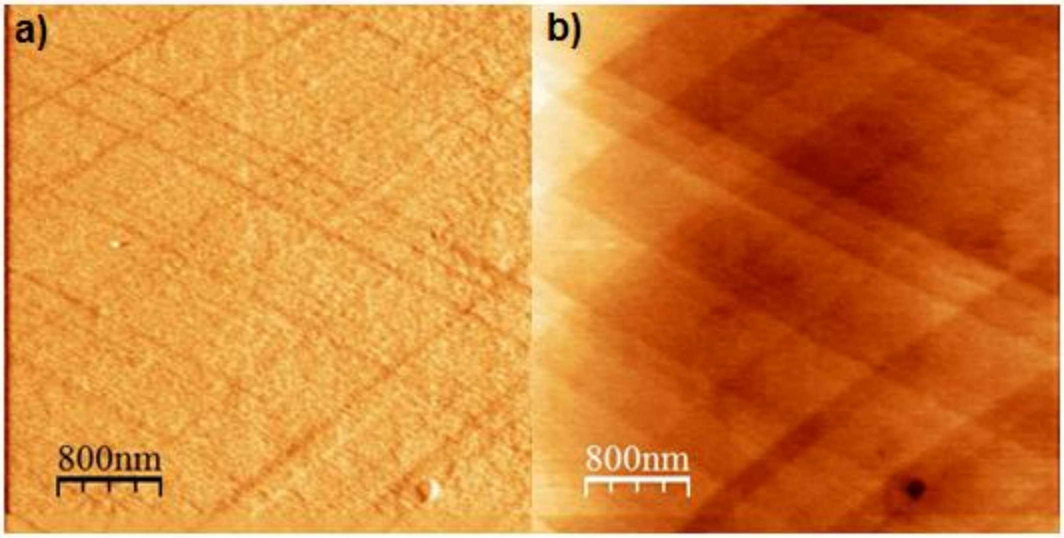

Figure 3.26. a) Initial error signal image and b) Initial topography image.

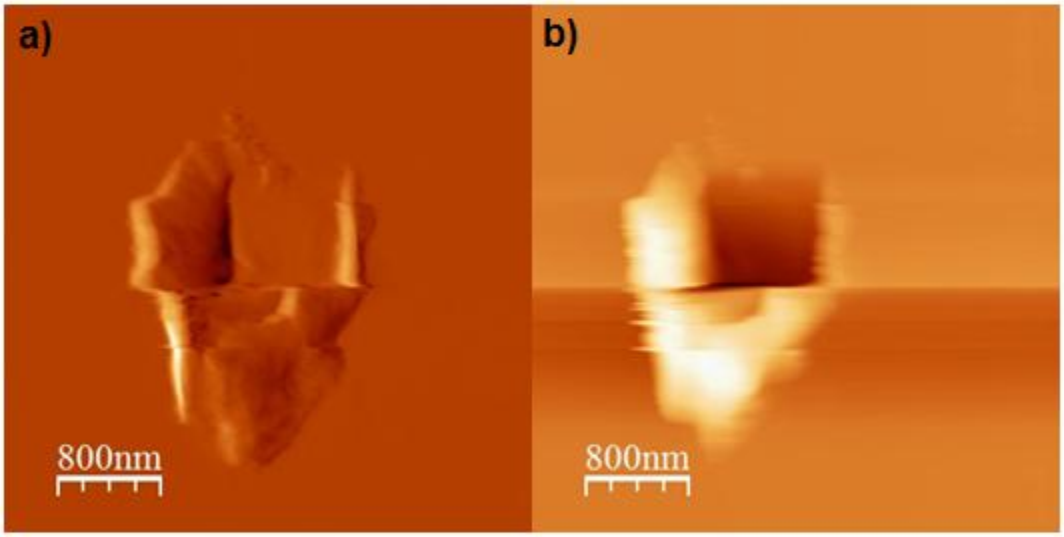

Figure 3.27. a) Error signal image showing the significant surface damage to the single crystal gold after 10 scans at 2 Hz speed with 1000 nN normal load and b) topography image.

The single crystal gold is inherently softer than the sputtered gold, as it has no grain boundaries to stop dislocations from propagating.

CHAPTER 4

ENVIRONMENTAL EFFECTS ON SCRATCHING

4.1 Introduction to Scratching

The motivation for experimenting with single pass scratches on gold was to observe if there was any correlation between the wear experiments performed both on the Hysitron Nanoindenter and the AFM. More specifically, to see if the same result of a higher wear rate, or in this case, scratch depth is achieved in experiments performed in water versus the ambient environment. It was also of interest to observe any differences when continually scanning over an area, versus a single pass scratch line.

4.2 Experimental Details of Scratching and Analysis

Tabor Shear/Scratch Tester was used in the following experiments on gold. The conical diamond tip was used for testing. This tip has a point diameter of 178 μm. The gold sample for testing was a 3 μm sputtered gold.

As the machine operates similar to a record player, some modifications had to be made for experiments to be carried out on smaller samples and to avoid putting holes in the center of the sample. A standard CD fits into the sample holder and the gold sample was mounted using cyanoacrylate (superglue). An example of this construction can be seen in Figure 4.1. To allow experiments to be performed in the presence of water, a plastic case was modified to fit on the scratch tester; equipped with a rubber gasket to prevent leakage into the machine. With this contraption, the CD with sample applied can be set into the plastic case and water can be poured in without damaging the machine.

Figure 4.1. The modifications performed to allow testing of small samples in the presence of water.

Ten single scratch scans were performed on the sample, 5 first in ambient conditions, and later 5 submerged in water. None of the additional weights available were applied to the support beam, making the effective load on the tip from the support beam itself 126 g.

A profilometer was used for analyzing the wear track after the experiment. The load of the stylus was 1 mg scanning at a speed of 50 μm/s.

4.3 Scratch Results

Before the profilometer scans were taken, images of the wear tracks were taken through an optical microscope. Figure 4.2 displays scans taken in the ambient environment. Figure 4.3 displays the scratches taken submerged in water.

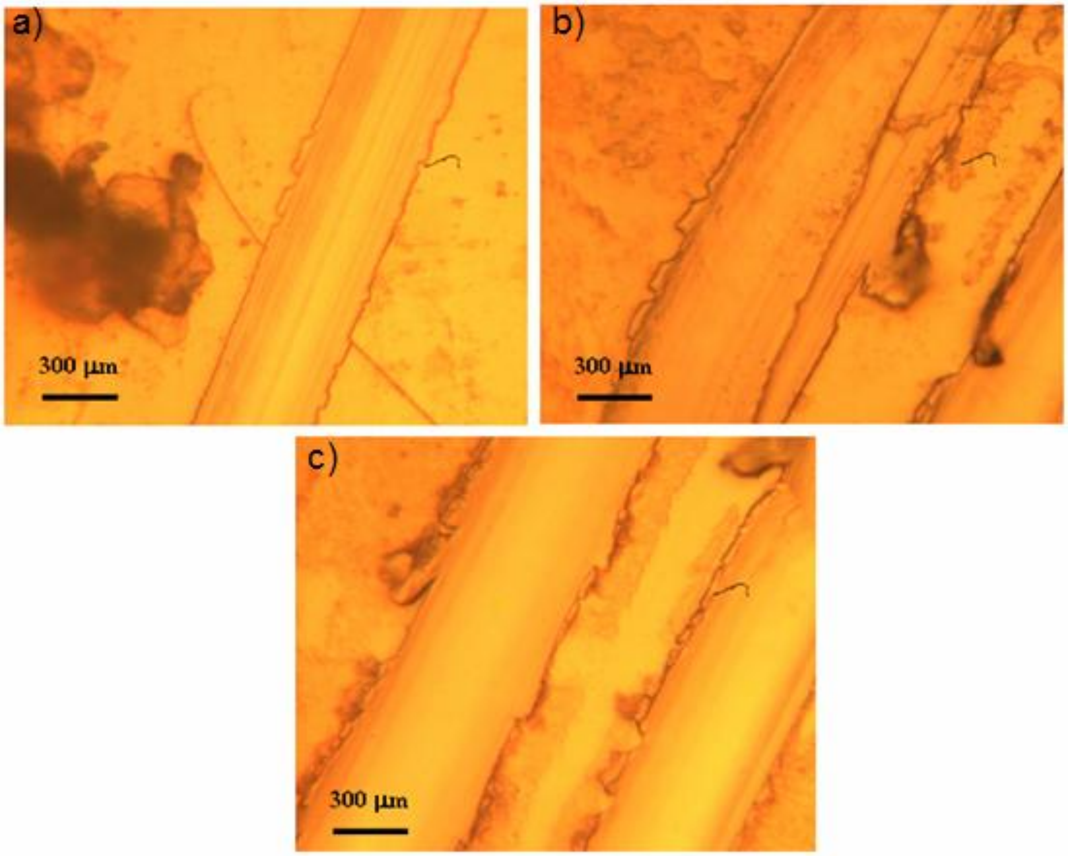

Figure 4.2. a), b), c) Single pass scratch lines performed in the ambient environment.

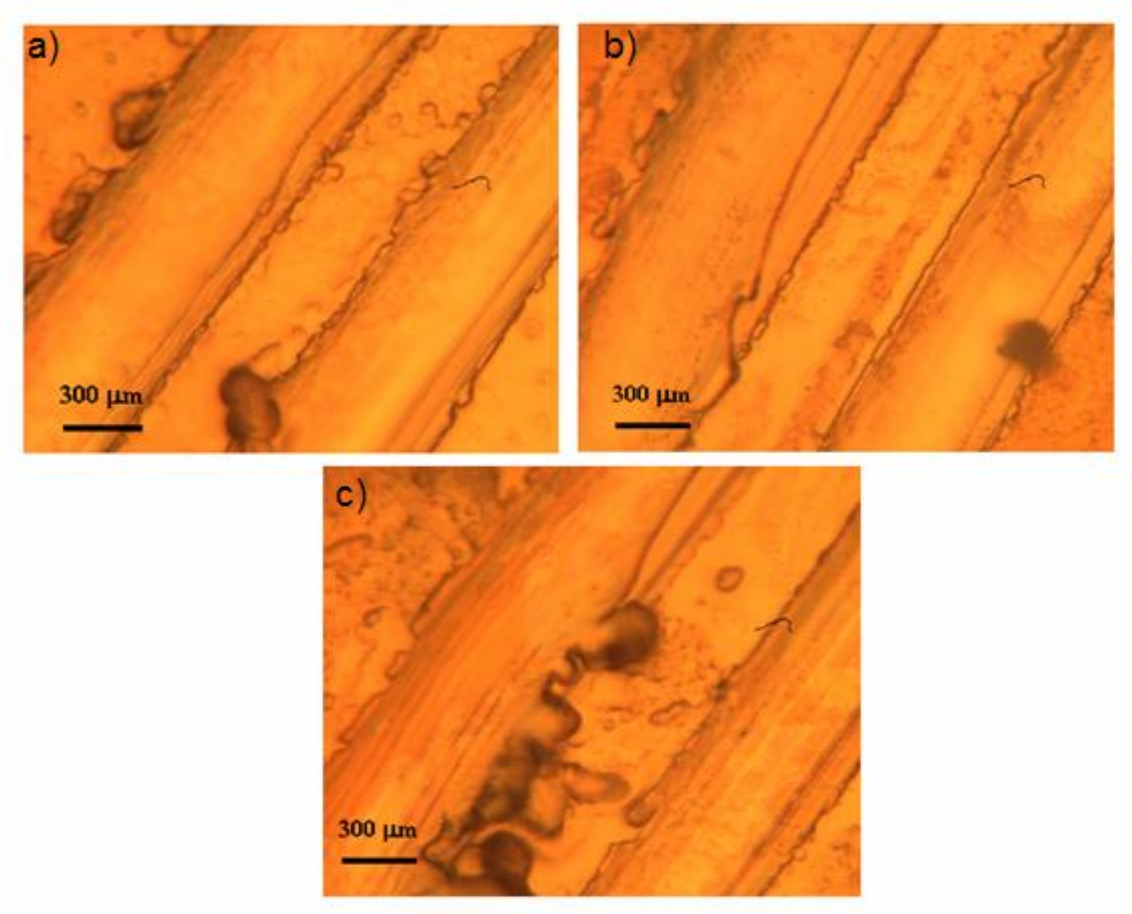

Figure 4.3. a), b), c) Single pass scratch lines performed submerged in water.

The texture of the scratches and outside pile up structures appears to be rougher in the wet scan images. There appears to be more microchipping in the area surrounding the scratch.

Profilometer scans provide quantitative data about the depth of the scan, as seen in Figures 4.4 and 4.5.

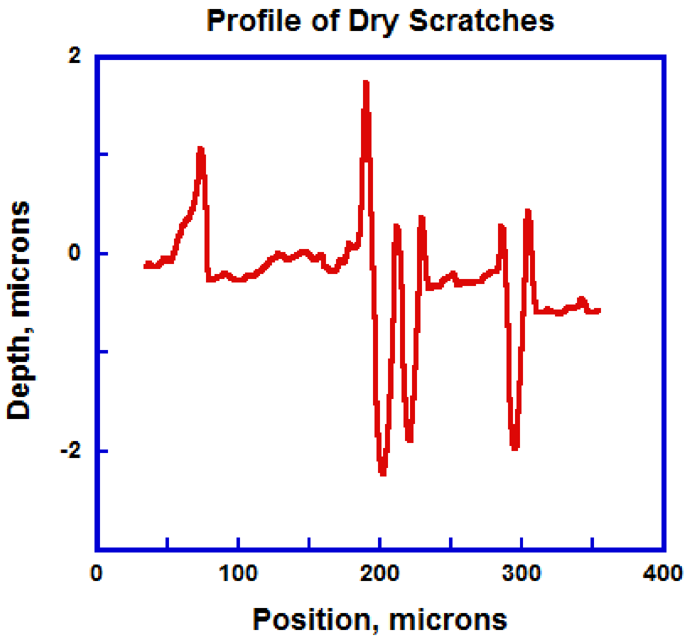

Figure 4.4. Depth profile of 3 scratches performed in ambient conditions. The average depth of the scratches is 2 μm.

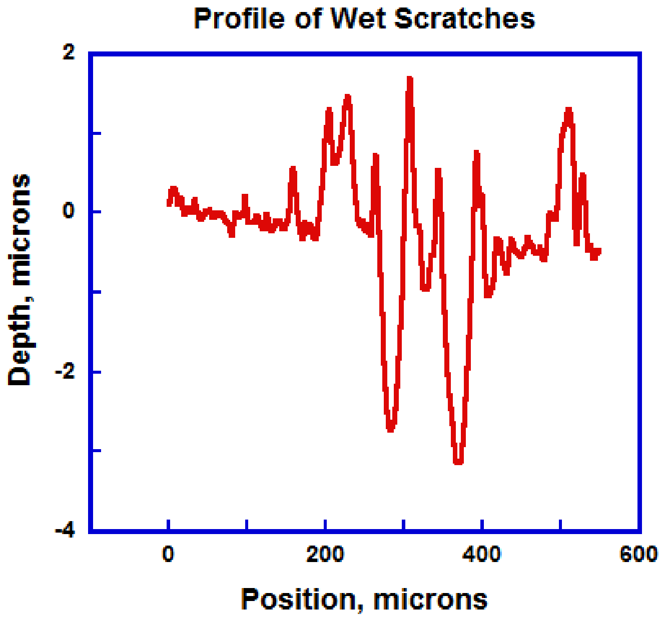

Figure 4.5 Depth profile of 2 scratches performed submerged in distilled water with all other parameters kept identical to experiments performed in ambient conditions. The average depth is 3 μm.

4.4 Scratch Analysis

The complicated nature of the wear process also extends into scratching, as there can be pure ploughing, sliding, fracture, delamination, or a combination of effects occurring. Figure 4.6 provides a schematic of some of the scratching effects.

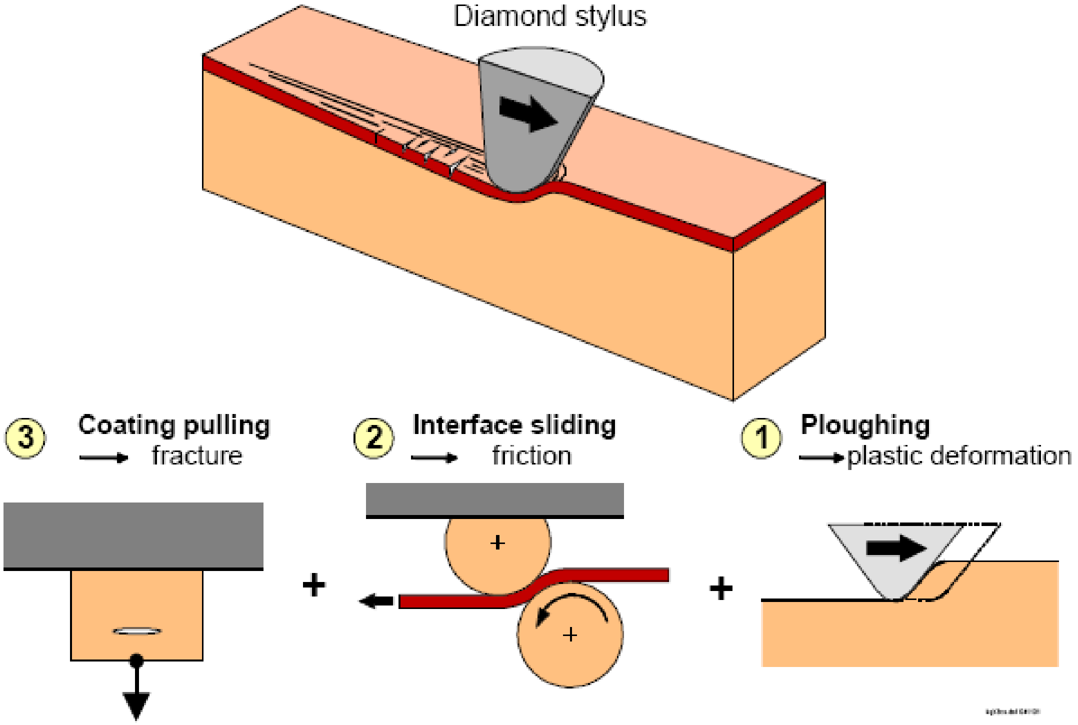

Figure 4.6. A schematic of the stylus traveling along a sample. Reproduced with permission from Holmberg, VTT, Netherlands.

Many material properties contribute to the behavior of a material subjected to scratching. It has been generally accepted that hardness correlates with wear resistance, however for coatings, the interfacial shear strength has been found to have a stronger effect [48]. The material's hardness is still a good indicator of the amount of plastic grooving, but the shear strength will predict chipping.

The wear mechanism for sputtered coatings has been found to be mainly microchipping and little coating detachment. This makes the shear strength even more influential to the gold's behavior. Tabor derived an equation using the shear strength to obtain the frictional force. From Tabor, the friction force can be divided into adhesion and ploughing:

$$F = \tau A_1 + pA_2 \tag{9}$$

In this equation for the frictional force (F), τ is the interfacial shear strength, A_1 is the projected contact area, p is the material flow stress represented by its hardness value, and A_2 is the projected cross sectional area of the scratch track.

Equations for the ploughing and adhesion coefficients (respectively) of friction have been derived by Bull [46]:

$$\mu_p = \left(\frac{2}{\pi}\right)\left(\frac{2r}{d}\right)^2 \left\{ \sin^{-1}\left(\frac{d}{2r}\right) - \left(\frac{d}{2r}\right)\left[1 - \left(\frac{d}{2r}\right)^2\right]^{\frac{1}{2}} \right\} \tag{10}$$

$$\mu_s = 2\left(\frac{2}{\pi}\right)\left(\frac{2r}{d}\right)^2 \left(\frac{\tau}{p}\right) \left\{ 1 - \left[1 - \left(\frac{d}{2r}\right)^2\right]^{\frac{1}{2}} \right\} \tag{11}$$

$$\mu_m = \mu_s + \mu_p \tag{12}$$

Where r is the indenter radius and d is the track width of the scratch. μ_m is the total coefficient of friction. As these experiments were performed at fairly low depths, the main component of friction should be due to the ploughing friction force according to previous experiments performed by others [46]. Scratches at relatively low depths means a smaller contact area; therefore less area for the adhesion component to play a role in friction. From the experimental data, the r value is 89 μm, and the track width, d = 25 μm for ambient air and d = 30 μm in water. The ploughing coefficient is the main contributor to the coefficient of friction in both cases. For the ambient air experiments: $\mu_p = 90.9$ and $\mu_s = 0.213$ and for the scratches submerged in water: $\mu_p = 69.2$ $\mu_s = 0.214$.

CHAPTER 5

CONCLUSIONS AND FUTURE WORK

5.1 Conclusions

This work has investigated ripple pattern formation during wear experiments on the micro and nanoscales. Experiments have also focused on the environmental effects of wear and scratch testing.

Successful reproduction of ripples produced in the UHV AFM was performed in the Hysitron nanoindenter and Park Scientific AFM on samples of KBr, single crystal Aluminum, sputtered and single crystal gold. The ripple's periodicity increases with the number of passes made on the sample as observed in other ripple pattern experiments as well. Many mechanisms have been studied as the possible cause of ripple pattern initiation, such as chatter, stick slip, and dislocation dynamics. The stick slip mechanism has been proposed as the primary source of ripple formation, and the exact cause is under investigation.

The addition of water to a wear experiment on gold produced considerably deeper wear areas than its ambient counterpart. Topography modification appears to be the main mechanism of ambient wear tests at the nanoscale, whereas much higher wear rate and nanoripples are observed in water. Moisture is influencing the material removal with increased wear rate. Most likely this moisture is assisting grain fracture and pull-off. In scratch testing on sputtered gold, the depth of scratch was found to be deeper in the presence of water than in ambient humidity, similar to the wear experiments.

5.2 Future Work

Much of this research was aimed at determining the types of materials and environmental conditions that would support pattern formation. Additionally, the material response to wear testing was determined. A valuable asset to the research surrounding the pattern formation would be a dynamics model of the system during scanning to observe what combination of parameters initiate the ripple pattern. Not only would modeling be useful in further understanding the pattern formation, but also to understand the wear process, and how it changes over time.

In terms of environmental effects, the development of a system to be able to test in a dry nitrogen (N_2) purged environment might elucidate interesting correlations between wear and relative humidity. It would also be of interest to observe if the viscosity of a liquid added to a wear test influenced the wear rate, or scratch depth at the micro and nanoscales. The behavior of materials at this reduced scale needs to be well understood before the potential of small scale devices can be realized.

REFERENCES

1. C. A. J. Putman, M. Igarashi, R. Kaneko, “Single-asperity Friction in force microscopy: The composite-tip model” Applied Physics Letters 66 23, pp. 3221-3227 (1995)
2. R. Carpick, “Controlling Friction” Science 313, pp. 184-185 (2006)
3. E. Meyer, E. Gnecco, “Skating on hot surfaces” Nature 6, pp. 180-181 (2007)
4. R. Carpick, M. Salmeron, “Scratching the surface: Fundamental investigations of tribology with atomic force microscopy” Chemical Review 91, pp. 1163-1194 (1997)
5. J. Celis, “A systems approach to the tribological testing of coated materials” Surface and Coatings Technology 74-75, pp. 15-22 (1995)
6. I. M. Hutchings, “Tribology: Friction and Wear of Engineered Materials” Edward Arnold, Publications Ltd., pp. 280-287 (1992)
7. K. Bowman, Mechanical Behaviors of Materials, Wiley, pp. 108-130 (2003)
8. A. Socoliuc, R. Bennewitz, E. Meyer “Ripple formation induced in localized abrasion” Physical Review B 68 115416 (2003)
9. M. Pendergast, R. Gunda, A. A. Volinsky, “Nanoripples Formation in Single Crystals” Materials Research Society Symposium Proceedings 1021 HH.5 (2007)
10. G. G. Adams, S. Muftu, N. M. Azhar, “A nano-scale multi-asperity contact and friction model” Journal of Tribology, ASME Transactions In Press (2002)
11. E. W. Deeg, “New algorithms for calculating Hertzian Stresses, Deformations, and contact zone parameters” AMP Journal of Technology 2, pp. 14-24 (1992)
12. D. S. Grierson, E. E. Flater, R. W. Carpick, “Accounting for the JKR-DMT transition in adhesion and friction measurements with atomic force microscopy” Journal of Adhesion Science Technology 19 3-5, pp. 291-311 (2005)
13. M. Surtchev, B. Jerome, “The initial stages of the wearing process of thin polystyrene films studied by atomic force microscopy” Nanotechnology 16, pp. 1213-1220 (2005)
14. A. Schumacher, E. Meyer, L. Scandella, “Influence of humidity on friction measurements of supported MOS_2 single layers” Journal of Vacuum Science Technology B 14 2, pp. 1264-1267 (1996)
15. J. A. S. Cleaver, L. Looi, “AFM Study of Adhesion between polystyrene particles;- the influence of relative humidity and applied load” Powder Technology 174, pp. 34-37 (2007)
16. D. Erts, A. Lohmus, R. Lohmua, H. Olin, A. V. Pokropivny, L. Ryen, K. Svensson, “Force Interactions and Adhesions of gold contacts using a combined atomic force microscope and transmission electron microscope” Applied Surface Science 188, pp. 460-466 (2002)

17. C. LaTorre, B. Bushan, “Investigation of scale effects and directionality dependence on friction and adhesion of human hair using AFM and macroscale friction test apparatus” Ultramicroscopy 106, pp. 720-734 (2006)
18. M. Paajanen, J. Katainen, O. H. Pakarinen, A. Foster, J. Lahtinen, “Experimental humidity dependence of small particle adhesion on silica and titania” Journal of Colloid and interface Science 304, pp. 518-523 (2006)
19. P. Bowden, D. Tabor, Friction, an Introduction to Tribology, Krieger Publishing (1982)
20. D. Karnopp, “Computer Simulation of stick-slip friction in mechanical dynamic systems” Transactions of the ASME 107, pp. 185-198 (1985)
21. R. W. Stark, G. Schitter, A. Stemmer, “Velocity dependent friction laws in contact mode atomic force microscopy” Ultramicroscopy 100, pp. 309-317 (2004).
22. B. Armstrong-Helouvry, P. Dupont, C. Canudas De Wit, “A survey of models, analysis tool and compensation methods for the control of machines with friction” Automatica, 30 7, pp. 1083-1994 (1994)
23. A. Meurk, “Microscopic stick-slip in friction force microscopy” Tribology Letters 8, pp. 161-169 (2000)
24. R. W. Stark, G. Schitter, A. Stemmer, “Velocity dependent friction laws in contact mode atomic force microscopy” Ultramicroscopy 100, pp. 309-317 (2004)
25. J. Schofer, E. Santner, “Quantitative wear analysis using atomic force microscopy” Wear 222, pp. 74-83 (1998)
26. J. Jiang, F. H. Stott, M. M. Stack, “Characterization of wear scar surfaces using combined three-dimensional topographic analysis and contact resistance measurements” Tribology International 30 7, pp. 517-526 (1997)
27. S. A. Whitehead, A. C. Shearer, D. C. Watts, N. H. F. Wilson, “Comparison of two stylus methods for measuring surface texture” Dental Materials 15, pp. 79-86 (1999)
28. A. Garbacz, L. Courard, K. Kostana, “Characterization of concrete surface roughness and its relation to adhesion in repair systems” Materials 56, pp. 281-289 (2006)
29. E. Gnecco, R. Bennewitz, A. Socoliuc, E. Meyer, “Friction and wear on the atomic scale” Wear 254, pp. 859-862 (2003)
30. B. Bhushan, D.R. Tokachichu, M.T. Keener, S.C. Lee, “Nanoscale adhesion, friction, and wear studies of biolmolecules on silicon based surfaces” Actabiolmaterialia 2, pp. 39-49 (2006)
31. Hysitron Inc., “Triboindenter users manual” (2003)
32. A. Socoliuc, E. Gnecco, R. Bennewitz, E. Meyer, “Ripple Formation Induced in Localized Abrasion” Physics Review B 68 115416 (2003)
33. M. Szymonski, F. Krok, B. Such, P. Piatkowski, J. J. Kolodziej, “Ripple Creation on InSb (001) Surface Ions vs. AFM Tip”, 3rd EFS Nanotribology Conference Proceedings 18-22 (2004)
34. U. Valbusa, C. Boragno, F. B. de Mongeot, “Nanostructuring Surfaces by Ion Sputtering” Journal of Physics: Condensed Matter 14, pp. 8153 (2002)
35. M. Navez, C. Sella, D. Chaperot, “Nonlinear Ripple Dynamics on Amorphous Surfaces Patterned by Ion Beam Sputtering” Czetch Republic Academy of Science 254 240 (1962)

36. Y. Nagamine, M. Hara, “Surface-element Analysis of Spatiotemporal Stripe Patterns Formed by Ag and Sb Coelectrodeposition” American Physical Society 68, pp. 298-308 (2005)
37. A. A. Volinsky, D.C. Meyer, T. Leisegang, P. Paufler, “Fracture Patterns in Thin Films and Multilayers” Materials Research Society Symposium Proceedings 795 U3.8 (2003)
38. A. Erdimir, “Review of engineered tribological interfaces for improved boundary lubrication” Tribology International 38, pp. 249-256 (2005)
39. M. Binggeli, C. M. Mate, “Influence of capillary condensation of water on nanotribology studied by force microscopy” Applied Physics Letters 65 4 (1994)
40. J. Barriga, Juarros A, Ahmed SI-U, J. L. Arana, “Microtribological analysis of gold and copper contacts” Tribology International In Press (2007)
41. R. G. Chadwick, H. L. Mitchell, I. Cameron, B. Hunter, M. Tulley, “Development of a novel system for assessing tooth restoration and wear” Journal of Dentistry 25, pp. 41-47 (1997)
42. R. Prehn, F. Haupert, K. Friedrich “Sliding wear performance of composites under abrasive and water lubricated conditions for pump applications” Wear 259, pp. 693-696 (2005)
43. P. Bertrand-Lambotte, J. L. Loubet, C. Verpy, S. Pavan “Understanding of automotive clear coats scratch resistance” Thin Solid Films 420-421, pp. 281-286 (2002)
44. L. Xu, H. Bluhm, M. Salmeron, “An AFM study of the tribological properties of NaCl (100) surfaces under moist air” Surface Science 407, pp. 251- 255 (1998)
45. A. Marti, G. Hahner, N. D. Spencer, “Sensitivity of frictional forces to pH on a nanometer scale: a lateral force microscopy study” Langmuir 11 12, pp. 4362-4365 (1995)
46. S. J. Bull, “Can Scratch testing be used as a model for the abrasive wear of hard coatings?” Wear 233-235, pp. 412-423 (1999)
47. J. von Stebut, “Multi-mode scratch testing – a European standards, measurements and testing study” Surface and Coatings Technology 200, pp. 346-350 (2005)
48. A. P. Tschiptschin, C. M. Garzon, D. M. Lopez, “The effect of nitrogen on the scratch resistance of austenitic stainless steels” Tribology International 39, pp. 167-174 (2006)
49. ASTM Standard designation: G 171-03
50. Y. Xie, H. M. Hawthorne, “On the possibility of evaluating the resistance of materials to wear by ploughing using a scratch method” Wear 240, pp. 65-71 (2000)
51. M. Wong, G. T. Lim, A. Moyse, J. N. Reddy, H. J. Sue, “A new test methodology for evaluating scratch resistance of polymers” Wear 256, pp. 1214-1227 (2004)
52. A. P. Tschiptschin, C. M. Garzon, D. M. Lopez, “The effect of nitrogen on the scratch resistance of austenitic stainless steels” Tribology International 39, pp. 167-174 (2006)
53. M. H. Wong, “The development of scratch test methodology and characterization of surface damage of polypropylene” Texas A&M University (2003)
54. Q. Zhao, Z. Zhao, E. Kazazic, M. Embree, P. Trinh, T. Lam, S. Chang, “Investigation of scratch resistance of thin carbon overcoat media using micro scratch testing” Wear 252, pp. 654-661 (2002)

55. J. C. M. Li, “Adhesive contact and scratch of polymer coatings” Materials Science and Engineering A317, pp. 197-203 (2001)
56. World Wide Web: http://www.eng.usf.edu/~volinsky/KBr.gif
57. A. Socoliuc, E. Gnecco, S. Maier, O. Pfeiffer, A. Baratoff, R. Bennewitz, E. Meyer, “Atomic scale control of friction by actuation of nanometer sized contacts” Science, 313, pp. 207-210 (2006)
58. M. Andersson, A. Iline, F. Stietz, F. Traager, “Formation of gold nanowires through self-assembly during scanning force microscopy” Applied Physics A: Material Science Process 68, pp. 609-614 (1999)
59. Quinn, G. D. "Hardness Testing of Ceramics” Advanced Materials and Processes 154 2, pp. 23-27 (1998)
60. P. Zelinski, “Chatter control for the rest of us” Modern Machine Shop Magazine (2005)
61. G. Tlusty, Manufacturing Processes and Equipment, Prentice Hall (2000)
62. R. W. Carpick, Q. Dai, D. F. Ogletree, M. Salmeron “Friction force microscopy investigations of potassium halide surfaces in ultrahigh vacuum: structure, friction and surface modification” Tribology Letters 5, pp. 91-102 (1998).
63. W. Y. H. Liew, “Effect of relative humidity on the unlubricated wear of metals”, Wear 260, pp. 720-727 (2006)
64. S. Cho, S. J. Kim, D. S. Lim, H. Jang, “Atomic Scale stick-slip caused by dislocation nucleation and propagation during scratching of a Cu substrate with a nanoindenter: a molecular dynamics simulation” Wear 259, pp. 1392-1399 (2005)
65. D. L. Woerdeman, J. A. Emerson, R. K. Giunta, “JKR contact mechanics for evaluating surface contamination on inorganic substrates” International Journal of Adhesion and Adhesives 22, pp. 257-264 (2002)
66. J. Jiang, M. M. Stack, “Modeling sliding wear: From dry to wet environments” Wear 261, pp. 954-965 (2006)
67. W. W. Gerberich, N. I. Tymiak, D. E. Kramer, “Fundamental Aspects of Friction and Wear Contacts in <100> surfaces” Material Research Society Symposium Proceedings 649, pp. 9.1.1-9.1.12 (2001)
68. K. Holmberg, A. Laukkanen, H. Ronkainen “Tribological optimization of coated components by stress modeling and surface fracture assessment” Tribology International In Press (2007)